Tectonomorphic scenarios in the Southern Alps of New Zealand

Frédéric Herman, Jean Braun, William J. Dunlap

Tectonomorphic scenarios in the Southern Alps of New Zealand

Frédéric Herman,[1,2] Jean Braun,[1,3] and William J. Dunlap[1]

[1]   Temperature-time histories of rocks are often used to constrain the kinematics of tectonic events, the evolution of landforms, erosion rates, and/or amount of faulting in tectonically active areas. However, interpretations based on thermal histories are not always straightforward as they rely on several interdependent mechanisms such as heat conduction, heat advection, or the presence of transient topography that must be taken into account. Using a three-dimensional finite element code recently developed by one of the authors, we have calculated temperature-time histories to interpret an existing thermochronological data set (K-Ar and FT) complemented by new low-T thermochronometer data ((U-Th)/He and FT) from the Southern Alps of New Zealand. Combined with inversion methods (Genetic Algorithm and Neighbourhood Algorithm), the model is used to derive from the data information on the tectonomorphic development of the orogen during the Pliocene and Pleistocene epochs. Assuming a quasi-geomorphic steady state, we can constrain the rate of tectonic horizontal advection and vertical uplift as well as the geometry of the main structural boundary, i.e., the Alpine Fault. We can also explain the along-strike geometry of the metamorphic isograds and thermochrons in relationship to surface topography. Furthermore, we show that if one assumes that the landscape has not been horizontally transported by tectonic movement, the relief on the west coast of the Southern Alps has increased. This relief increase could have been initiated at any time between 1.5 Ma and 100 ka. Any relief reduction during this period is ruled out by our modeling. Alternatively, if the landscape is advected horizontally in the direction normal to the trace of the Alpine Fault, a relief increase is not required to explain the thermochronological data.

1.   Introduction

[2]   Mountain building is a dynamical process that results from the combination of crustal shortening, vertical thickening and erosional processes [e.g., *Adams*, 1980; *Jamieson et al.*, 1998; *Koons*, 1987; *Molnar and England*, 1990; *Avouac and Burov*, 1996; *Beaumont et al.*, 2001]. As a mountain belt grows, stream channels and hillslopes become steeper, precipitation is orographically enhanced and in turn erosion increases. The geomorphic expression of the mountain belt therefore represents the dynamical (dis)equilibrium between erosion and tectonics. In recent years, many have tried to determine the rate at which landforms can respond to external changes (i.e., climate and/or tectonics changes) and whether steady state landforms can exist [*Willett et al.*, 2001; *Montgomery*, 2001; *Whipple et al.*, 1999]. While it is broadly agreed that many active orogens, including the Southern Alps of New Zealand [*Adams*, 1980; *Batt*, 1997; *Willett and Brandon*, 2002] or the Olympic Mountains [*Montgomery*, 2001], have approached a regional topographic steady state it is, however, unlikely that a balance between erosion and tectonic uplift is ever reached at all points of the landscape. This is the case because the structural architecture of developing orogens evolves through time, and the surface must necessarily react to the formation of new structures, across many timescales. In addition, because of the nonlinear behavior of erosional processes, interpretation of the evolution of the topography on tectonic timescales (Myr) is not obvious and most attempts have so far relied on a priori models for fluvial/glacial/hillslope erosion and transport processes [*Molnar and England*, 1990; *Whipple et al.*, 1999]. Similarly, thermochronological data used to quantify erosion rates have often been inappropriately collected to constrain the evolution of the shape of the landform [*Tippett and Kamp*, 1995; *Batt*, 1997]. We present here a thermochronological data set that has been purposely collected in the Southern Alps of New Zealand to provide direct estimates on the rate of landform change. We show that by coupling strategic

---

[1]Research School of Earth Sciences, Australian National University, Canberra, ACT, Australia.
[2]Now at Geological and Planetary Science Division, California Institute of Technology, Pasadena, California, USA.
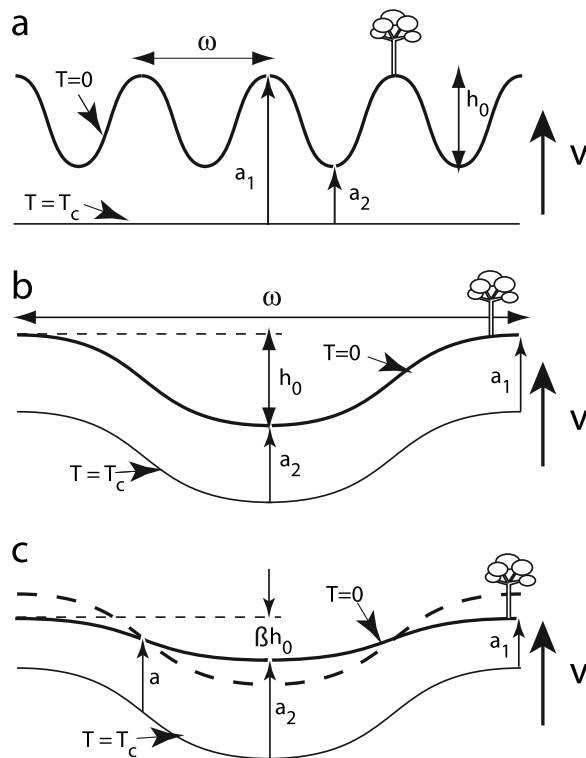[3]Now at Géosciences Rennes, Université de Rennes 1, Rennes, France.

Figure 1. Age-elevation relationships that can be observed at different wavelengths (ω) [*Braun*, 2003]. T is the temperature and h is the altitude. (a) Short-wavelength topography does not affect the geometry of closure temperature isotherm, T_c, and the slope of the age-elevation, a versus h, relationship gives the inverse of the exhumation rate, v, ($\partial a/\partial h = a_1 - a_2/h_0 = 1/v$). (b) Long-wavelength topography strongly affects the shape of the T_c isotherm, and age is independent of elevation ($\partial a/\partial h = 0$) (c) At long topographic wavelengths, any age variation with elevation is indicative of a relative change (β) in relief amplitude since rocks crossed the T_c isotherm.

sampling and analysis with numerical techniques, one can constrain the rate of evolution of the topographic surface which can in turn be used to calibrate surface processes models.

[3] Low-temperature thermochronology broadly has been used to infer information on the evolution of topography in different tectonic settings [e.g., *Brown et al.*, 1994; *Brandon et al.*, 1998; *Braun*, 2002b]. Age-elevation relationships (AERs) are commonly used to derive exhumation rates (Figure 1). However, the temperature structure of the uppermost crust is strongly influenced by the presence of finite amplitude topography [*Turcotte and Schubert*, 1982; *Stüwe et al.*, 1994; *Stüwe and Hintermüller*, 2000] and care must be taken while interpreting AERs. *Braun* [2002b] showed that depending on the wavelength of topography one will observe different responses. Indeed, for a given thermochronometer, (1) short-wavelength topography does not affect the geometry of the closure temperature isotherm and the slope of AER gives us an estimate of the exhumation rate (Figure 1a), whereas (2) long-wavelength topography strongly affects the shape of the closure temperature

isotherm so that any spatial variation in age is likely to be indicative of a relative relief change (Figures 1b and 1c). Therefore, by having a good representation of the evolution of the geothermal gradient (e.g., using an appropriate thermal model) to determine an adequate sampling strategy and collect data at an appropriate wavelength for the topography, one can quantify the evolution of landforms using low-temperature thermochronology. This is the method we are using in this study.

[4] We first give an overview of the Southern Alps of New Zealand and present a new data set using (U-Th)/He and fission track dating techniques. Making use of previously published thermochronological ages, we derive information on the three-dimensional (3-D) thermal state of the Southern Alps of New Zealand based on the predictions of a 3-D kinematic thermal model (Pecube) [*Braun*, 2003] and discuss some of the implications derived from the model. New (U-Th)/He in zircon as well as fission track in zircon and apatite ages are then used to derive direct estimates on the development of the present-day surface topography. We interpret the evolution of the landscape using two independent methods: (1) the 3-D thermal model [*Braun*, 2003] and (2) a spectral analysis of the AER [*Braun*, 2002a].

2. Southern Alps of New Zealand

[5] The collision zone is viewed as incorporating the central mountain range (i.e., the Southern Alps) and its flanking Canterbury and Westland sedimentary basins. This prominent mountain range results from ongoing oblique thrusting of the Pacific plate crust over the Australian plate crust [*Sutherland*, 2000] predominantly along a single crustal-scale structure, the Alpine Fault [*Wellman*, 1979] (Figure 2).

2.1. Geodynamical Models of the Southern Alps

[6] It is commonly assumed [*Wellman*, 1979] that the mantle part of lithosphere of the incoming Pacific Plate delaminates, with material from above 25 km depth advected to the surface along the Alpine Fault, while lower crustal material is either added to the orogenic root or subducted with the Pacific lithospheric mantle (Figure 3). This scheme is supported by geological and geophysical evidence and GPS measurements [e.g., *Allis*, 1981, 1986; *Craw et al.*, 1994; *Stern*, 1995; *Davey et al.*, 1995; *Beavan et al.*, 1999; *Kleffmann et al.*, 1998; *Molnar et al.*, 1999; *Norris and Cooper*, 2000; *Little and Holcombe*, 2002].

[7] Geodynamical models, based on geophysical investigations (Figure 3a [*Stern et al.*, 2001]), structural geology (Figure 3b [*Little and Holcombe*, 2002]) and numerical simulations (Figure 3c [*Batt*, 1997]), suggest that subduction within the mantle lithosphere leads to the development of two major oppositely dipping shear zones in the crust [*Willett et al.*, 1993; *Koons*, 1994; *Little and Holcombe*, 2002]. This model is known as the doubly vergent critical wedge model [*Koons*, 1990]. One of these shear zones, termed the retro-shear zone [*Willett et al.*, 1993] develops into a major crustal-scale thrust structure, comparable in scale and position to the Alpine Fault. The other, the pro-shear zone [*Willett et al.*, 1993] develops at approximately 45° in the opposite direction. The position of this zone
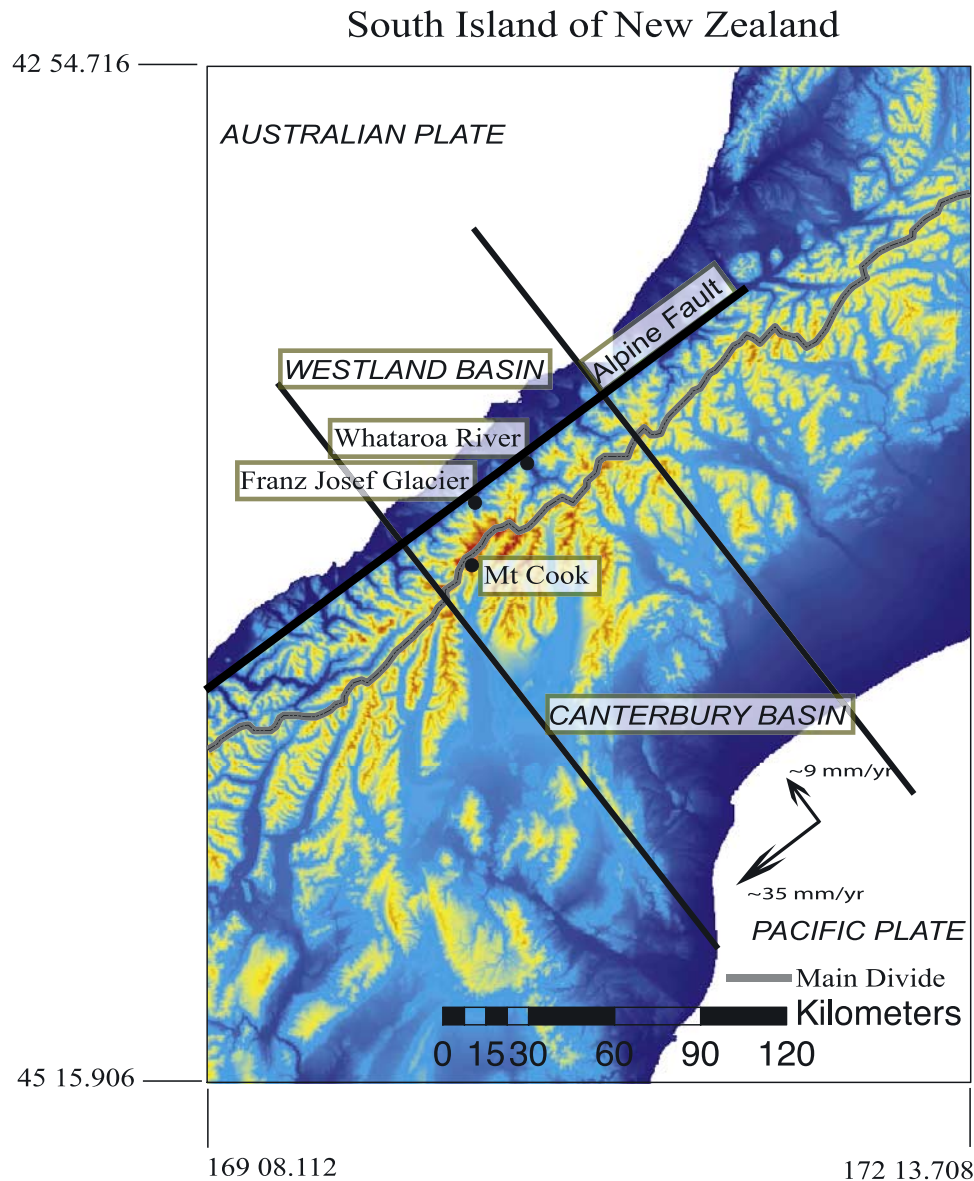
South Island of New Zealand

Figure 2. Digital image (Terralink) of the South Island of New Zealand. The focus of this study is the central part: the Southern Alps. The two flanking basins catch sediment shed from either side of the divide. Whatoaro River, Franz Josef Glacier, and Mount Cook are also located.

where strain accumulates stays unchanged as the model develops, but rocks advect through this feature toward the center of the wedge. This style of crustal deformation is very similar to that proposed by *Wellman* [1979] many years ago.

2.2. Geologic Setting

[8] The geology of the Southern Alps is largely described in a number of recent papers [e.g., *Norris et al.*, 1990; *Chamberlain et al.*, 1995; *Walcott*, 1998; *Beaumont et al.*, 1996; *Batt*, 1997]. Some specific aspects useful for this study are detailed here and summarized in Figures 3 and 4.

[9] The Alpine Fault (Figure 3) is generally considered as the boundary between the Pacific and the Indo-Australian plates. This S-E dipping (~50° [*Sibson et al.*, 1979]) dextral-reverse oblique structure is traceable in refraction and reflection seismic surveys to at least 22 km depth

[*Davey et al.*, 1995; *Smith et al.*, 1995]. However, in detail, the Alpine Fault is not a single continuous feature, but consists of N-S trending zones dominated by oblique over-thrusting, alternating with more E-W trending zones of predominantly strike-slip displacements [*Norris et al.*, 1990]. This partitioning is, however, limited to the top 1–2 km of the crust [*Norris and Cooper*, 2000].

[10] The distribution of metamorphic grades has been interpreted as a reflection of differential exhumation rates across the orogen. The Alpine Schists are exposed in a narrow belt southeast of the Alpine Fault [*Tippett and Kamp*, 1995]. They comprise low- to high-grade Triassic foliated metagraywacke, sandstone and argillite [*Andrews et al.*, 1976] initially deformed and metamorphosed during the Jurassic-Cretaceous Rangitata orogeny [*Grindley*, 1963] and subsequently during the ongoing Kaikoura orogeny [*Findley*,
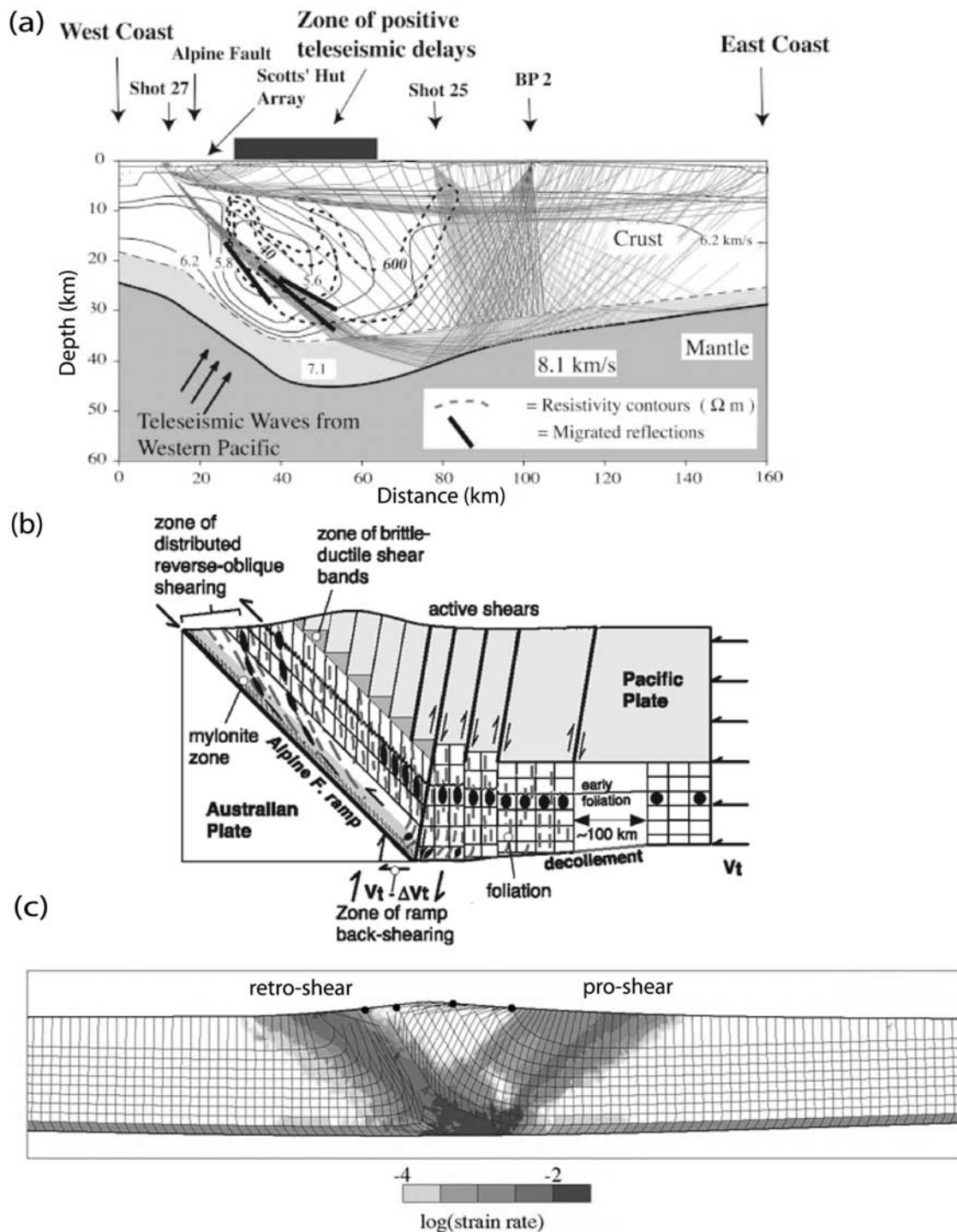
Figure 3. (a) Crustal model with waves speed and apparent conductivity superimposed from [*Stern et al.*, 2001]. (b) Crustal model from structural observation from *Little and Holcombe* [2002]. (c) Doubly vergent orogen model from *Batt* [1997].

1987; *Grapes and Watanabe*, 1983]. Midamphibolite facies rocks adjacent to the Alpine Fault are progressively replaced by greenschist facies rocks (through biotite and chlorite zones), pumpellyite-actinolite and ultimately prehnite gray-wacke facies rocks with increasing distance from the Alpine Fault [*Turner*, 1933; *Mason*, 1962].

[11] A major fault system known as the Main Divide Fault Zone of the Southern Alps [*Cox and Findley*, 1995] is observed within the deformed zone of the Pacific Plate, east of the Main Divide. This fault system dips steeply N-W and extends 60 km along strike (Figures 4 and 3b). The Main Divide Fault Zone is being continually uplifted and carried westward, while new faults form in the same position at depth [*Cox and Findley*, 1995]. The present exposure is therefore thought to be only the most recent expression of this structural feature, with some schist fabrics between the
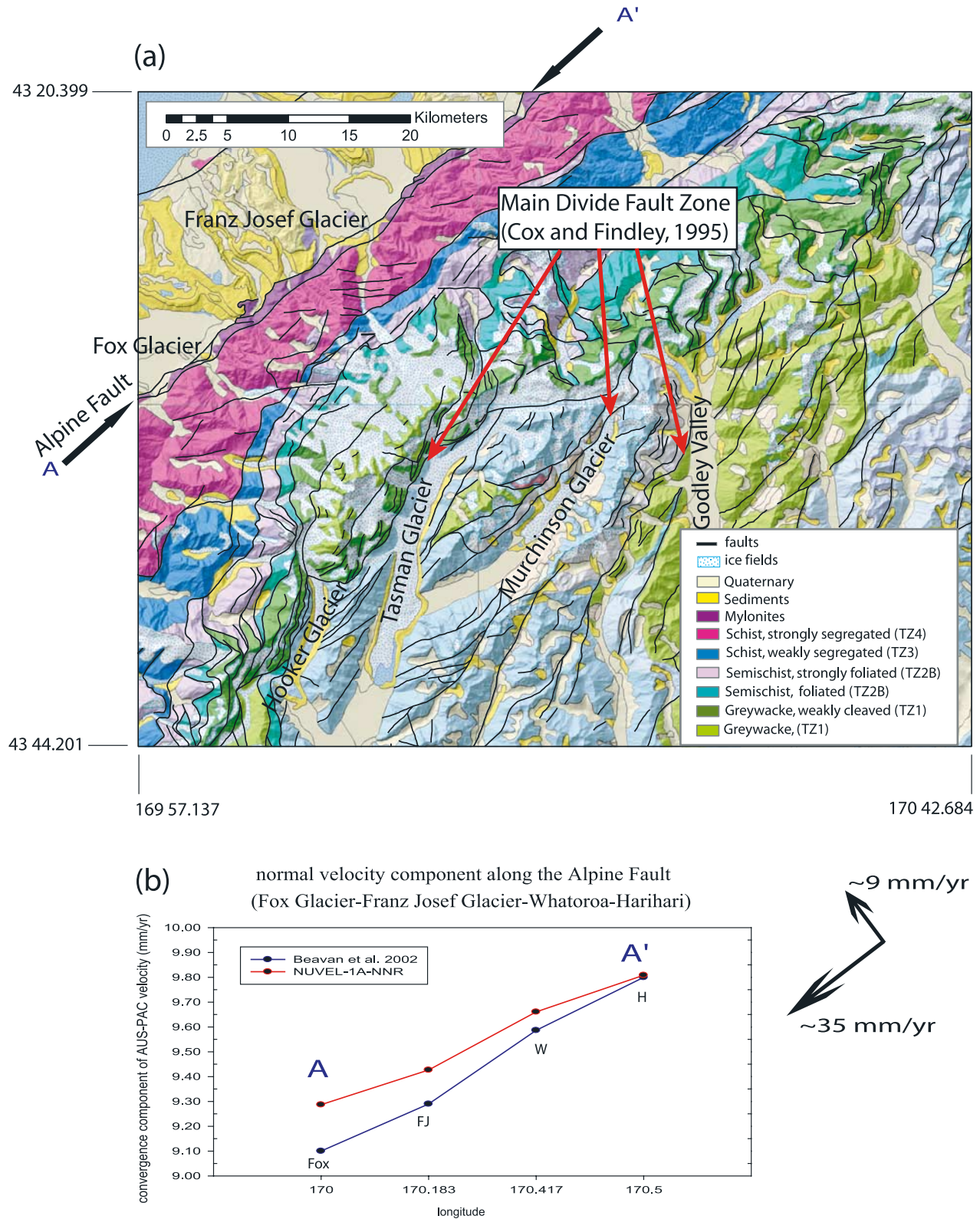
Figure 4. (a) Outline of the major geological features of the central part of the South Island of New Zealand. Major structural zones are illustrated (S. Cox, personal communication, 2002). (b) Variation in the convergent component of relative PAC-AUS plate velocity. Euler vectors are inferred from *Beavan et al.* [2002] and NUVEL-1A. Velocities are drawn with increasing longitude from A to A', going from south west to north east along the Alpine Fault.
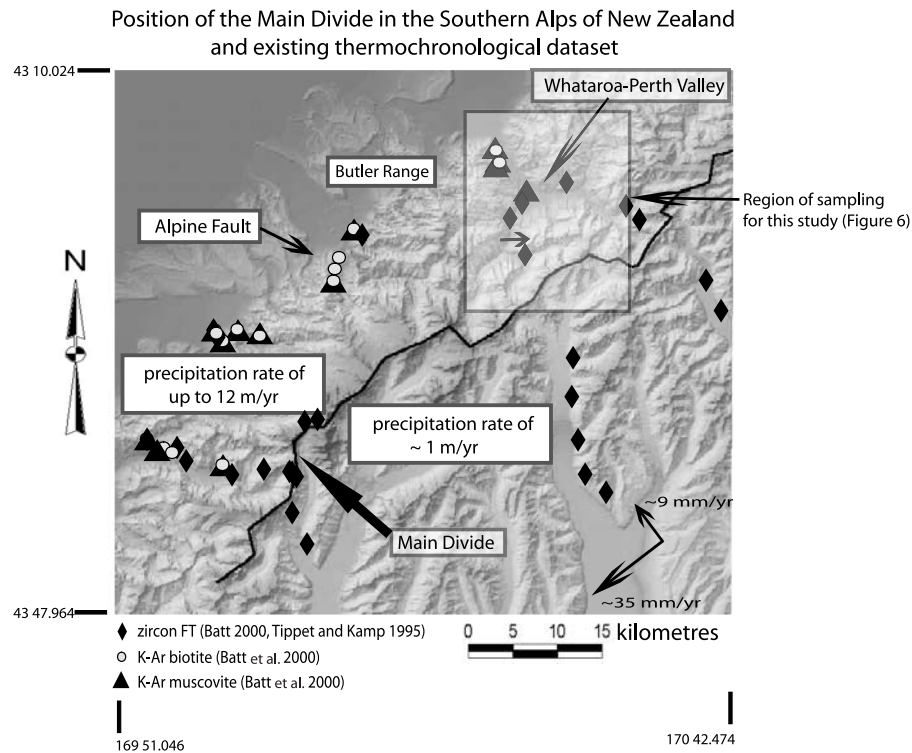
Figure 5. Main Drainage Divide approximates the orographic barrier that induces the rain shadow effect (maximum precipitation being focused on the western side). Segmentation into 10 to 30 km lengths is observed for the position of the divide with regard to the Alpine Fault. Locations of existing thermochronological data are also shown: FT in zircon from *Batt et al.* [2000] and *Tippett and Kamp* [1995], as well as K-Ar in Muscovite and Biotite [*Batt et al.*, 2000]. The topography is extracted from a 50 m digital elevation model (Terralink).

Main Divide Fault Zone and the Alpine Fault possibly representing deeper equivalents of former Main Divide faults now uplifted and exhumed by movement on the Alpine Fault and erosion [*Cox and Findley*, 1995].

2.3. Geomorphologic Setting

[12] The Southern Alps exhibit a strong asymmetry in both topography and exhumation. West of the Main Divide, mean surface elevation decreases rapidly toward the Alpine Fault. Surface elevation is unrelated to lithological variation or to total rock uplift [*Tippett and Kamp*, 1995]. In contrast, east of the Main Divide the regional slope is gentler, with elevation proportional to a rock exhumation as determined by the interpretation of fission track data [*Tippett and Kamp*, 1995]. The Southern Alps are characterized by asymmetrical precipitation patterns as they represent an orographic barrier to the predominant westerly winds, resulting in orographically enhanced rainfall (up to 12 m yr^{-1}) on the west coast [*Griffiths and McSaveney*, 1983], and a corresponding rain shadow effect on the east coast. Figure 5 illustrates the location of the Main Drainage Divide which approximates the orographic barrier that induces the rain shadow effect. The position of the divide with regard to the Alpine Fault is characterized by segmentation of 10 to 30 km length segments subparallel to the fault.

[13] The Southern Alps are characterized by a mixture of fluvial and glacial landforms. *Adams* [1980] suggested that glacial erosion may deepen and widen valleys, but may remove little material from the valley slopes, whereas interglacial erosion concentrates on valleys sides. *Whitehouse* [1987] described regions on the western side of the main divide as a fluvial-dominated landscape (where V-shaped valleys have formed in response to intense fluvial dissection, landsliding, and rockfall-snow avalanching), evolving toward a more glaciated landscape toward the main drainage divide (characterized by the presence of steep back-walled cirques) and an "older glacial landscape" on the southeastern side of the divide dissected by long, linear, U-shaped glacial valleys. It is, however, clear that the geomorphology of the western side of the Southern Alps is best described as "transitional" between glacial and postglacial conditions [*Whitehouse*, 1987]. Although today's landscape shows fluvial characteristics, there are indications that components of the landscape on the west coast are glacial in origin as evidenced by the presence of glacial relics [*Porter*, 1975; *Willett*, 1950; *Adams*, 1980; *Whitehouse*, 1987; *Suggate*, 1990].

2.4. Geophysical Constraints

[14] Anomalously high heat flow measurements from drill holes (190 ± 50 W m^{-2} in the Franz Josef, 4 km SE to the Alpine Fault [*Shi et al.*, 1996], 90 ± 25 W m^{-2} in the Haast area and up to 76 ± 15 W m^{-2} west of the Alpine Fault [*Townend*, 1999]) are commonly interpreted as a consequence of the high exhumation rates southeast of the Alpine Fault [e.g., *Shi et al.*, 1996; *Batt and Braun*, 1997, 1999].

[15] Between 1994 and 2002 repeated GPS geodetic measurements have been performed on the South Island [*Beavan et al.*, 1999]. Contemporary velocity and strain rate fields derived from these observations are largely invariant along the northeasterly strike of the mountain range and Alpine fault. Across strike, inversion of contemporary strain estimates suggest that 60–70% of the relative surface plate boundary motion is accommodated by the Alpine Fault. These geodetic data also suggest that a section of the Alpine Fault is currently creeping beneath 5–8 km depth [*Beavan et al.*, 1999].

[16] A broad negative isostatic gravity anomaly extends for 150–200 km along the Southern Alps [*Allis*, 1981, 1986; *Stern*, 1995]. Interpreted in conjunction with other factors [*Reyners*, 1987; *Reyners and Cowan*, 1993; *Smith et al.*, 1995], this marked gravity anomaly is seen to reflect the presence of up to 80 km of subducted lithospheric mantle [*Stern*, 1995].

[17] Recent deep seismic velocity models along transects in the central South Island provide an image of a 30 km thick crustal root [*Davey et al.*, 1995; *Stern et al.*, 2000]. *Davey et al.* [1995] identify the Alpine Fault as a moderately dipping (30–40°) low seismic velocity zone that extends to about 30–35 km depth (Figure 3a). The upper mantle structure beneath the Southern Alps has been investigated by *Stern et al.* [2000]. Interpreting teleseismic P wave arrival patterns, a high-velocity symmetric zone has been evidenced, leading *Molnar et al.* [1999] and *Stern et al.* [2000] to suggest that following continental convergence, the lithosphere has been homogeneously shortened and thickened rather than subducted. However, *Pysklywec et al.* [2002] reconciled these apparently contradicting scenarios by suggesting that during the early stages of collision the system may evolve from uniform thickening to subduction-like behavior.

2.5. Thermochronological Constraints

[18] Numerous studies have made use of thermochronology to improve our understanding of the dynamic history of the orogen [*Adams and Gabites*, 1985; *Kamp and Tippett*, 1993; *Batt et al.*, 2000]. *Adams and Gabites* [1985] were the first to describe a pattern common to most thermochronometers in which young ages are associated with the present-day Kaikoura (or Alpine) orogeny and within 10 km of the Alpine Fault, whereas old ages associated with the Triassic to Cretaceous Rangitata orogeny are found further than 25 km from the Alpine Fault.

[19] Several investigations have focused on the fission track dating method [*White and Green*, 1986; *Kamp and Tippett*, 1993; *Tippett and Kamp*, 1995]. Such data sets provide good constraints on shallow crustal behavior because of the low closure temperature of the fission track system for apatite, in the range of 110–125°C [*Gleadow and Duddy*, 1981; *Green et al.*, 1989], and zircon, 240–265°C [*Hurford*, 1990].

[20] *Batt et al.* [2000] established ages for the K-Ar system in biotite and muscovite and fission track in zircon and apatite throughout the orogen, providing insights into the earlier stages of the dynamic development of the orogen. *Batt* [1997] showed that in most parts of the Southern Alps an exhumational steady state has developed over the last 5 Myr, reflecting a balance between heat conduction and advection by uplift and erosion. Most of the thermochronological data sets have been collected along river channels on either sides of the divide [*Kamp and Tippett*, 1993; *Batt et al.*, 2000] making them unsuitable for constraining the age of the landform [*Braun*, 2002a, 2002b]. To remedy this problem, we performed additional sampling centered around the upper reaches of the Whataroa and Perth rivers.

3. Samples and Analytical Method

3.1. Study Area and Samples

[21] Sampling has been carried out along a 16 km transect near-parallel to the Alpine Fault, across the Whataroa-Perth catchment (Figure 6) which forms one of the main basin on the west side of the orogen. The Whataroa-Perth catchment is an attractive site because this region has experienced substantial denudation and is the locus of maximum exhumation rate in the entire orogen, i.e., up to 8–13 mm yr^{-1} [e.g., *Batt and Braun*, 1997; *Walcott*, 1998; *Norris and Cooper*, 2000]. Sampling has been performed within the upstream part of the Whataroa and Perth rivers. The length of the transect and sample spacing were chosen to provide information on the evolution of the landform in the area (see *Braun* [2002a] for a complete discussion on sampling strategy for dating landform evolution). As shown on the topographic (Figure 6) and geologic maps (Figure 4 (S. Cox, IGNS)), sampling has mainly been done within the same textural zone (textural zone 2B, adopting the textural divisions defined by *Turner* [1933]). The sampled rocks are schist of greenschist facies. Zircon is fairly abundant (largest grains were handpicked for (U-Th)/He dating). These detrital zircons show large variations in shape as well as in U and Th concentration. Cathodoluminescence imaging revealed grains of many shapes and internal zonation. We suspect that zonation as well as nonperfect grain geometry are the most likely candidate as the cause of poor age reproducibility. Detrital apatites are less abundant and usually very small. For this reason, only fission track dating was possible on some of the samples.

3.2. (U-Th)/He Dating Method

[22] Zircon (U-Th)/He ages were measured on aliquots of 3 to 7 grains. Dated crystals were handpicked from separates using a microscope and screened for large inclusions and appropriate shape to permit the calculation of the α ejection correction. Crystals were loaded in platinum foil tubes that were heated for 15 to 20 min at 1250°C using a Nd:YAG low-blank (typically $\leq 3 \times 10^{-16}$ mol over 25 min on masses 3 and 4) helium line at the Research School of Earth Sciences (RSES), Australian National University (ANU). Temperatures were controlled using an optical pyrometer. The evolved gas was purified by getters and measured by ^{3}He isotope dilution using a sensitivity-mapped quadrupole mass spectrometer. Crystals were reheated at a similar temperature to ensure complete extraction of helium. The reproducibility of the standard ^{3}He spike was tested before and after most of the measurements. Once retrieved from the line, crystals were dissolved in Teflon bombs using a HNO_3 and HF mixture. Uranium and thorium were measured by ^{233}U isotope dilution using an Agilent inductively coupled plasma–mass spectroscopy (ICP-MS). Correction for α ejection was done using the
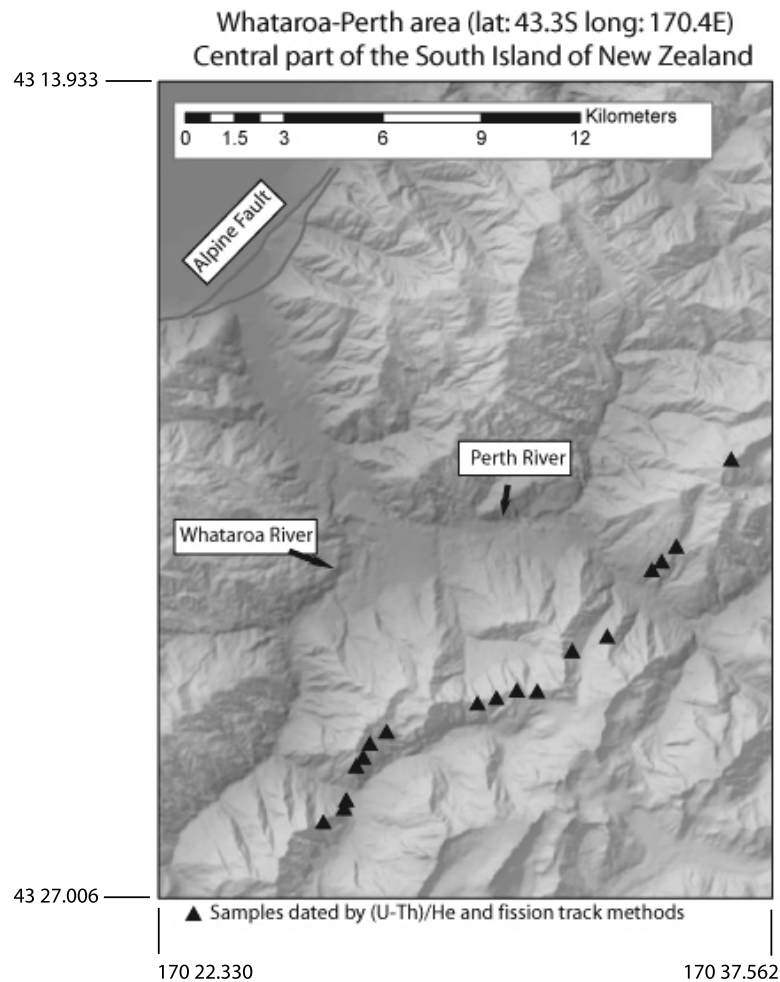
Figure 6. Location of the transect near-parallel to the Alpine Fault where the new thermochronological data have been sampled (Terralink).

zircon method described by *Farley* [2002]. The total analytical uncertainty in each analysis (±3–4%) is dominated by the precision of the He (including mass discrimination) and U and Th measurements. Most of the samples were analyzed in duplicate to ensure a reproducibility of ages within 5–15%. The errors reported here are a combination of analytical error and variability among replicates (i.e., the standard error given is the square root of the sum of the squared standard deviations).

3.3. Fission Track Dating in Zircon and Apatite

[23] Apatites were mounted in epoxy, polished and etched in a 1M HNO_3 solution at 20°C for 50 s. Zircons were embedded in Teflon, polished and etched in a eutectic NaOH-KOH melt at 228°C for 6 to 8 hours. All samples were dated by the external detector method, using a zeta calibration factor for Fish Canyon and Durango age standards [*Hurford*, 1990]. Samples were irradiated at the well-thermalized ORPHEE facility of the Centre d'Etudes Nucléaires in Saclay, France, with a nominal fluence of 2.5 Å1015 neutrons cm^{-2}. Neutron fluences were monitored using CN1 and NBS962 dosimeter glasses. All samples were dated at the Laboratoire des Chaînes Alpines, Université Joseph Fourier Grenoble (France).

3.4. Helium Diffusion Behavior of Zircon

[24] Previous diffusion experiments suggest that zircon He loss may obey an Arrhenius relationship [*Reiners et al.*, 2002, 2004], except for the early stages of step heating where the fraction of gas released is negligible. *Reiners et al.* [2004] concluded that non-Arrhenius trends in the early stages would have a negligible effect on the bulk thermal sensitivity and proposed a closure temperature window of 170–190°C (with a cooling of 10°C Myr^{-1}), with $E_a = 39$–41 kcal mol^{-1}, $D_0 = 0.09$–1.5 cm^2. We are using the mean value of these constants (i.e., $E_a = 40.4$ kcal mol^{-1}, $D_0 = 0.46^{0.87}_{-0.30}$ cm^2 [*Reiners et al.*, 2004]) to interpret our ages.

3.5. Measured Ages

[25] The new thermochronologic data obtained in this study are presented in Tables 1 and 2 and Figure 7. The transect crosses two valleys in the upstream part of the Whataroa-Perth catchment: the first part of the transect crosses the Butler River and the second part the Perth River. The measurements indicate that the ages are young enough to be associated with the ongoing Kaikoura orogeny (i.e., all less than 5 Ma). Average ages for the Perth and Butler transects are close enough to assume that the mean exhumation rate is similar in both parts of the profile; indeed

Table 1. Measured (U-Th)/He Zircon Ages[a]

ANU Sample	Latitude	Longitude	N	2R	R, μm	Mass, μg	^{238}U, ppm	^{232}Th, ppm	U/Th	Ft	^{4}He, nmol/g	Age NC, Ma	Age C, Ma	Mean Age, Ma	2σ Error, Ma
amu-05079	43 21.640	170 33.628	6	134.17	67.085	74.7	145.9	25.3	5.8	0.82	1.2	1.51	1.84	1.81	0.07
			6	106	53	47.6	410.1	61	6.7	0.78	3.09	1.39	1.77		
amu-05081	43 25.295	170 26.375	2	117.5	58.75	22.3	649.3	92.2	7	0.8	2.44	0.69	0.86	0.86	0.04
amu-05067	43 24.480	170 26.938	5	87.5	43.75	28	111.6	25	4.5	0.75	0.6	0.98	1.31	1.47	0.17
			4	93.4	46.7	17.4	389.1	52.4	7.4	0.75	2.58	1.22	1.64		
amu-05063	43 23.708	170 30.741	5	146	73	81.1	399.6	12.7	31.5	0.83	4.95	2.34	2.81	2.81	0.09
amu-05087	43 21.770	170 33.404	5	141	70.5	90.3	216	56.7	3.8	0.83	2.97	2.46	2.95	3.01	0.16
			5	112.8	56.4	55.8	317.4	67.8	4.7	0.8	4.3	2.46	3.07		
amu-05072	43 25.533	170 26.313	4	118.75	59.375	45.8	517.6	94.1	5.5	0.81	3.95	1.39	1.73	1.69	0.11
			4	127	63.5	53.5	461.8	41.9	11	0.82	3.33	1.34	1.64		
amu-05086	43 19.988	170 35.253	4	132.13	66.065	49	369.7	74.6	5	0.82	2.23	1.09	1.34	1.39	0.1
			6	99.17	49.585	32.8	435.7	70.1	6.2	0.76	2.62	1.1	1.45		
amu-05060	43 23.878	170 29.383	6	110.83	55.415	47	80.6	47.2	1.7	0.79	0.6	1.24	1.58	1.81	0.25
			4	140	70	65.1	78	2.9	26.7	0.83	0.7	1.7	2.05		
amu-05077	43 22.837	170 32.352	5	114.1	57.05	37.9	290.5	45.2	6.4	0.79	2.05	1.3	1.64	1.59	0.08
			4	138.125	69.0625	50.5	204	50.1	4.1	0.82	1.42	1.25	1.53		
amu-05068	43 24.702	170 26.768	4	93	46.5	14.8	626.9	398.1	1.6	0.74	3.49	0.92	1.25	1.36	0.14
			3	98	49	15	667.3	127.4	5.2	0.76	4.1	1.12	1.48		
amu-05088	43 25.434	170 26.310	5	99	49.5	29.2	226.9	52.4	4.3	0.77	1.11	0.88	1.15	1.15	0.16
amu-05069	43 24.843	170 26.608	5	93.1	46.55	21.6	236.2	153.5	1.5	0.74	1.11	0.77	1.04	0.98	0.08
			5	108.2	54.1	37.1	428.2	126.8	3.4	0.78	1.75	0.73	0.93		
amu-05061	43 23.793	170 29.817	5	127	63.5	55.4	122.7	34.1	3.6	0.81	0.67	0.98	1.21	1.25	0.11
			4	156.25	78.125	76	186.9	18.4	10.1	0.84	1.09	1.08	1.29		
amu-05062	43 23.808	170 30.280	4	113.2	56.6	24.3	268	230.9	1.2	0.77	2.83	1.66	2.15	2.03	0.14
			6	109	54.5	40.1	124.7	36.2	3.4	0.78	1.04	1.48	1.9		
amu-05075	43 23.062	170 31.548	6	89	44.5	22.6	132.9	23.9	5.6	0.74	0.89	1.22	1.65	1.65	0.08
amu-05082	43 21.297	170 33.959	7	131.43	65.715	84.3	273.9	41.5	6.6	0.82	1.93	1.3	1.59	1.8	0.25
			4	111.25	55.625	41.7	232.7	104.9	2.2	0.8	2.18	1.61	2.02		

[a]N, the number of crystals; R, the mean radii; α, ejection; Ft, corrected following the method described by *Farley* [2002]; NC, not corrected; C, corrected.

Table 2. Measured Fission Track Ages in Zircon[a]

ANU Sample	N	$\rho_s(N_s)$, $\times 10^5$ cm^2	$\rho_i(N_i)$, $\times 10^5$ cm^2	$\rho_\delta(N_\delta)$, $\times 10^5$ cm^2	P(χ^2), %	U, ppm	Age, Ma	Error, Ma
anu05-072	20	17.3(282)	73.7(1200)	1.11(15917)	84.2(12.94)	288	1.9	0.1
anu05-069	20	22.8(398)	103(1799)	1.11(15917)	11.5(26.57)	358	1.6	0.1
anu05-079	11	19.6(152)	86.2(796)	1.11(16698)	18.5(13.75)	309	1.8	0.2
anu05-079	47	0.56(53)	43.2(4090)	5.97(17676)	97.8(28.76)	9	1.3	0.2
anu05-087	20	11.8(238)	83.7(1695)	1.11(15917)	92.4(10.99)	303	1.1	0.1
anu05-082	20	19.0(375)	71.5(1415)	1.11(15917)	100.0(2.36)	240	2.2	0.1
anu05-086	20	15.9(152)	83.2(796)	1.11(15917)	96.3(9.56)	333	1.5	0.1

[a]N, number of grains counted; ρ_s, spontaneous track density; ρ_i, induced track density; ρ_d, dosimeter track density; Ns, Ni, Nd, number of tracks counted to determine the reported track densities; P(χ^2), chi-square probability that the single grain ages represent one population; U (ppm) is the uranium concentration.

these are located at a similar distance from the main thrust, the Alpine Fault. Most of the (U-Th)/He ages lead to a good agreement with fission track measurements, except for one sample (anu-05087, Table 1) where the fission track age in zircon is younger than the (U-Th)/He age in zircon. This age is reported here but left aside in our interpretation.

4. Numerical Method and Age Data Interpretation

[26] In this section, we present the numerical model used for our interpretation, describing its underlying assumptions, required input and consequent output. The general objective is to simulate the thermal state of the crust with time and extract T-t paths from which ages can be calculated.

4.1. Solving the Heat Transfer Equation (Pecube)

[27] Previous work has highlighted the effect of small-amplitude surface topography on the steady state thermal structure of the crust [*Turcotte and Schubert*, 1982; *Stüwe et al.*, 1994; *Stüwe and Hintermüller*, 2000]. Furthermore, as outlined in the introduction, it is unlikely that in an actively deforming mountain belt a true topographic steady state is ever reached at all timescales [e.g., *Willett and Brandon*, 2002]. Consequently, in order to use low closure tempera-

ture thermochronometric systems to determine the age of a landscape and potentially its rate of change, the effects of finite amplitude, transient surface topography on the temperature structure of the upper crust must be taken into account.

[28] We achieve this by solving the transient, three-dimensional heat transfer equation:

$$\rho c \left(\frac{\partial T}{\partial t} + v_h \frac{\partial T}{\partial x} + v_s \frac{\partial T}{\partial y} + v_z \frac{\partial T}{\partial z} \right)$$
$$= \frac{\partial}{\partial x} k \frac{\partial T}{\partial x} + \frac{\partial}{\partial y} k \frac{\partial T}{\partial y} + \frac{\partial}{\partial z} k \frac{\partial T}{\partial z} + \rho A \quad (1)$$

where $T(x, y, z, t)$ is the temperature, ρ is rock density, c is heat capacity, v_h, v_s and v_z are horizontal and vertical velocities, k is conductivity and A is radioactive heat production per unit mass. Equation (1) must be solved for a given initial temperature field:

$$T_0 = T_0(x, y, z, t = 0) \quad (2)$$

and a set of boundary conditions:
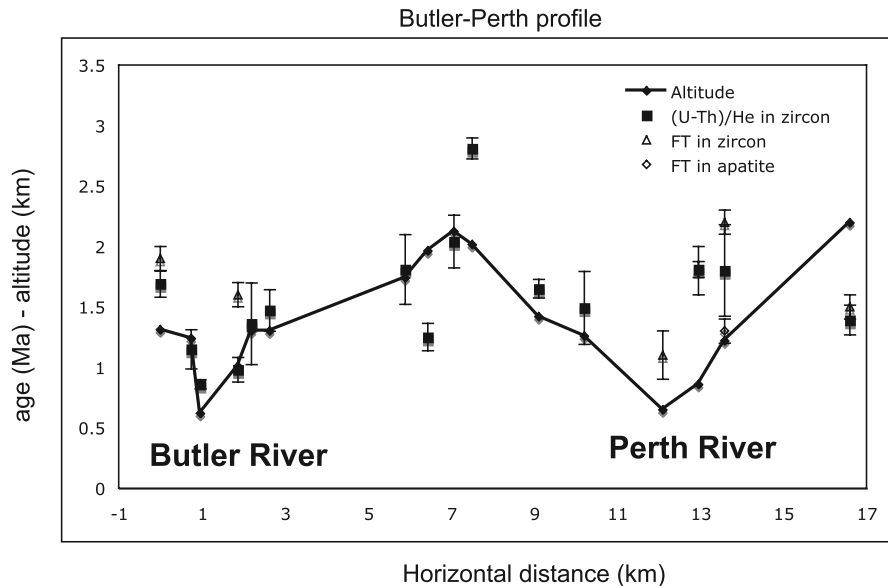
$$T(x, y, z = z_0, t) = T_b \quad (3)$$

Figure 7. Summary of all the ages measured. x axis is the horizontal distance (km), y axis is elevation (km) and age (Ma).

$$T_s(x, y, z = S(x, y, t), t) = 0 \qquad (4)$$

$$\frac{\partial T(x = x_0, x_l, y = y_0, y_l, z)}{\partial n} = 0 \qquad (5)$$

where $z = z_0$ represent the base of the crust and $S(x, y, t)$ is the surface topography. *Braun* [2003] developed a finite element code (Pecube) that solves equation (1) within a crustal block. This code is used here to simulate the evolution of the temperature field beneath the Southern Alps of New Zealand. Unlike other models of its kind [e.g., *Ehlers et al.*, 2003], Pecube includes the effects of time varying surface topography.

[29] Assuming the thermal properties of the crust, the model mostly requires two inputs: (1) the model is only kinematic, so that a velocity field must be assumed and (2) a geomorphic scenario must be supposed. For the models presented herein, the thermal properties and boundary conditions of the crustal block are as follows: T_b is equal to 500°C, thermal diffusivity ($K = k/\rho c$) of 25 km^2 Myr^{-1} and radioactive heat production (A/c) of 28.8°C Myr^{-1}. Using Pecube, we can predict temperature-time histories (T-t) for rocks that are exhumed and brought to the surface, assuming the tectonic model as well as the geomorphic evolution of the topographic surface. These T-t paths are in turn used to calculate ages for each thermochronometric system investigated (the methods used to calculate the apparent ages from each thermochonometer are briefly outlined below).

[30] For this study, we have modified Pecube to include horizontal motion. Our velocity model represents crustal deformation by movement along the Alpine Fault and assumes horizontal transport and vertical uplift that are coupled to ensure mass conservation. The derivation of the velocity field is based on the "rule of the normal" [*Braun et al.*, 1994] which is a simple kinematic model based on the assumption that lines within the hanging wall initially normal to the fault remain so following deformation. In our model, the depth (Ψ (km)) of the Alpine fault is represented by an exponential of the form (Figure 8)

$$\Psi = \left[\exp\left(\frac{-x}{\lambda}\right) - 1 \right] h \qquad (6)$$

x (km) is the horizontal distance east of the surface trace of the Alpine Fault, h (km) is the thickness of the deforming layer (i.e., depth of the decollement) and λ (km) is the listricity. Furthermore, in order to include a drag along the fault, we introduce an extra parameter F (km). When F is equal to zero, the velocity is taken equal to v_h everywhere along the line normal to the fault; v_h (mm yr^{-1}) is the convergence component of velocity of the Pacific Plate with respect to the Alpine Fault. For F greater than 0, the velocity is given by $\sqrt{(F - \zeta)/F} v_h$ between [0, F] (ζ is the distance from the fault) and is equal to v_h for ζ larger than F (Figure 9a). The velocity field is shown in Figure 8. The resulting rock paths are similar to those predicted from the doubly vergent critical wedge theory [*Koons*, 1990; *Willett et al.*, 1993].

(a) Velocity field derived from the rule of the normal
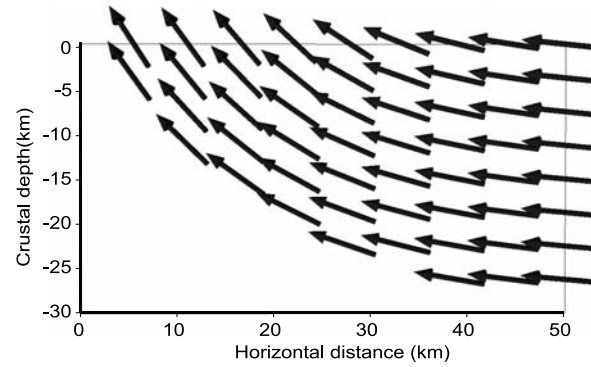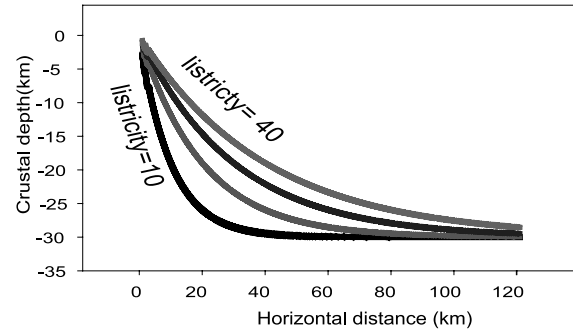

(b) Fault geometry

Figure 8. (a) Assumed velocity field in a crustal block obtained by applying the rule of the normal [*Braun et al.*, 1994]. The rule of the normal assumes that lines within the hanging wall that are normal to the fault before deformation remain so following deformation. (b) Geometry adopted for the shape of the Alpine Fault.

4.2. From Temperature to Ages

[31] In our model from each T-t path an age can be calculated. K-Ar biotite and muscovite ages are computed by solving the solid-state production-diffusion equation for a given geometry using a finite difference scheme:

$$\frac{\partial C}{\partial t} = D\nabla^2 C + P \qquad (7)$$

C is the concentration of Ar and P is its production rate. $D(t)$ is the time-dependent diffusion coefficient obeying the following Arrhenius relationship:

$$\frac{D}{a^2} = \frac{D_0}{a^2} \exp\left(\frac{-E_a}{RT}\right) \qquad (8)$$

where D_0 is the diffusivity at infinite temperature, E_a is the activation energy, R is the gas constant, T is the temperature, and a is the diffusion domain radius. We adopt the diffusion characteristics of biotite derived by *Harrison et al.* [1985] ($E_a = 47$ kcal mol^{-1}, $D_0/a^2 = 342$ s^{-1} and a diffusion geometry that is cylindrical) and tested by *Dunlap* [2000]. The diffusion properties for muscovite have been investigated by several groups and still remain unclear [*Dodson*, 1973; *Hames and Bowring*, 1994; *Kirschner et al.*, 1996; *Dunlap et al.*, 1991]. Here we use diffusivities calculated by
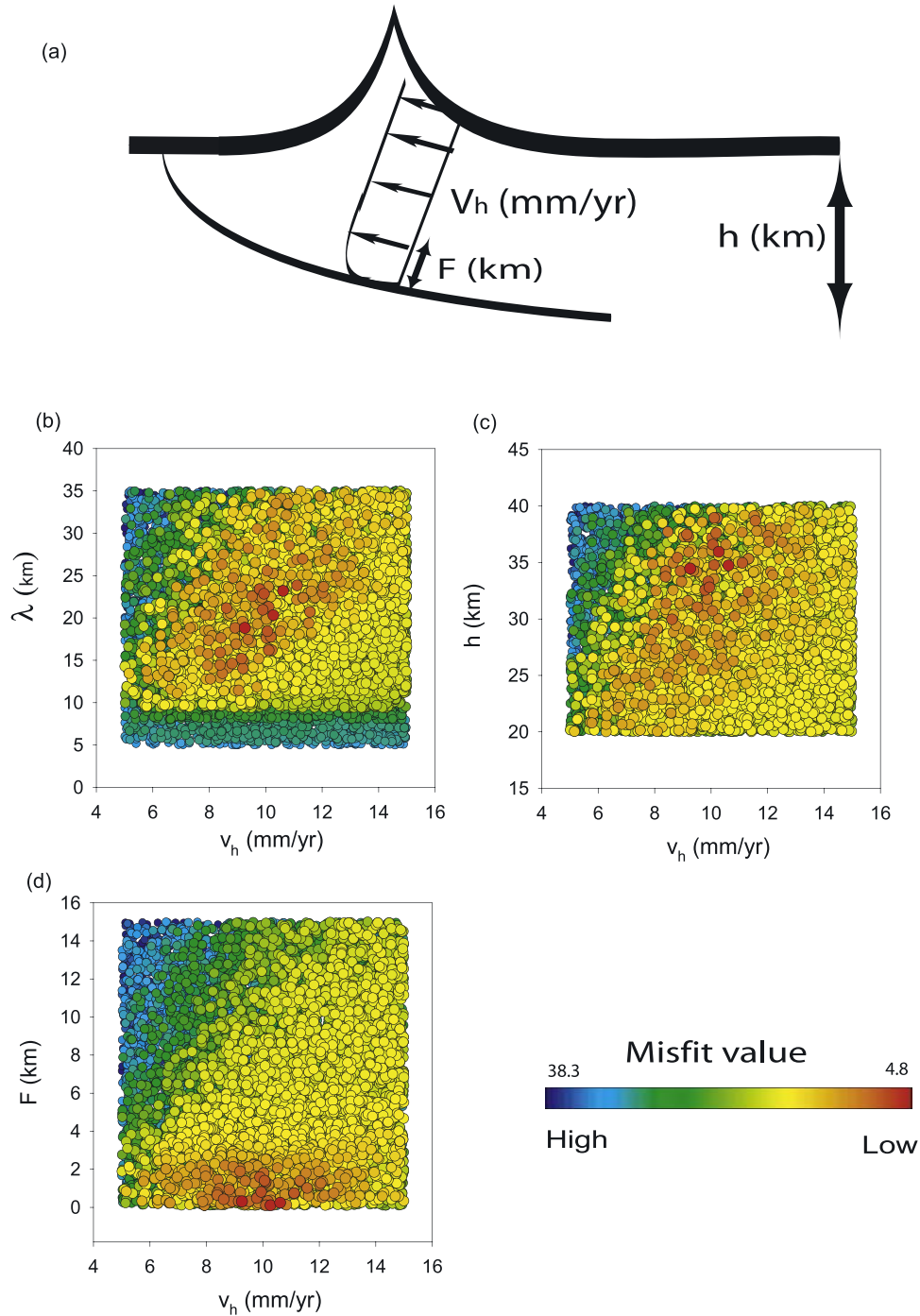
Figure 9. (a) Geometrical parameters that we invert using Pecube and the Genetic Algorithm (see text). Figures 9b, 9c, and 9d are 2-D projections of the results. The red dots mean low misfit, i.e., predicted and observed ages are similar, whereas the blue ones mean high misfit value. (b) The v_h, convergence velocity, versus λ, fault listricity. By looking at the red dots, a trade-off appears between these two parameters: if the velocity decreases the fault must flatten (i.e., λ increases). (c) The v_h versus h, the thickness of the crust above decollement. A trade-off appears between these two parameters, for the red dots. (d) F must be minimized.

Hames and Bowring [1994] ($E_a = 52$ kcal mol^{-1}, $D_0/a^2 = 0.24$ s^1 and a diffusion geometry that is cylindrical). On the contrary, zircon fission track ages are much less straightforward to model. This is mainly due to the lack of a well-defined mechanism describing the annealing of tracks in zircon [*Zaun and Wagner*, 1985; *Brandon and Vance*, 1992; *Brandon et al.*, 1998; *Tagami et al.*, 1990]. To circumvent these difficulties, we calculate an effective diffusion model using diffusivities that would lead to a closure temperature of ~230–250°C as suggested by *Batt* [1997]

Numerical models and age data interpretation			
section	aim	method	data used
5.1	Put constraints on the kinematic settings	Pecube + GA	Tippett and Kamp, 1995; Batt et al 2000
5.2	Consequence of the kinematic model in the direction perpendicular to the Alpine Fault	Pecube	
5.3	Consequence of the kinematic model along strike	Pecube	
5.4	Put constraints on the evolution of the landform	Pecube + NA	(U-Th)/He and FT ages presented in this study
5.5	Effects of advection of the landscape	Pecube	(U-Th)/He and FT ages presented in this study
6	Quantify landform change	Spectral analysis	(U-Th)/He and FT ages presented in this study

Figure 10. Sequence in which our analysis of the tectonomorphic evolution of the Southern Alps is presented. See text for explanation on Pecube, the GA and the NA in the text.

(E_a = 49.77 kcal mol^{-1}, D_0/a^2 = 6406.25 s^{-1} and a diffusion geometry that is cylindrical).

5. Numerical Model Results

[32] In this section, we first show models at the scale of the orogen in a bid to constrain the regional tectonics of the Southern Alps, using previously published thermochronological data sets [*Tippett and Kamp*, 1995; *Batt et al.*, 2000]. We then use these constraints to discuss more detailed synthetic models to help understand the impact of along-strike topography on the age distribution for low-temperature thermochronometers. Finally, using the constrained kinematic model, we focus on the evolving topography and propose an interpretation for the new (U-Th)/He in zircon and fission track in zircon and apatite ages in terms of landform evolution. The sequence in which we present our analysis of the tectonomorphic evolution of the Southern Alps is presented in Figure 10.

5.1. Constraints on the Kinematic Part of the Model

[33] To constrain the large-scale thermal development of the orogen, we use Pecube to compare predicted ages to ages reported by *Kamp and Tippett* [1993] and *Batt* [1997]. Our aim is to constrain the geometry of the Alpine Fault and the convergence rate of the Pacific plate toward the Australian plate. The comparison is optimized by making use of an inversion method. The method used in the section is a gradient free search strategy based on the well known Genetic Algorithm (GA) [*Holland*, 1975; *Goldberg*, 1989]. The objective is to produce an ensemble of models by varying model parameters namely λ, the listricity of the

Alpine Fault, v_h, the convergence velocity, F, the drag coefficient along the fault and h, the thickness of the layer being deformed.

[34] The degree of fit of the model relative to the data is estimated through a misfit function which is defined as

$$\frac{1}{n} \sum \frac{\sqrt{(x_i - y_i)^2}}{\sigma_i} \qquad (9)$$

where x_i are observations and y_i are synthetic ages calculated with Pecube, n is the amount of samples and σ_i is the error associated with the ages (note that for K-Ar ages the error was arbitrarily set to 10% since only analytical errors were reported by *Batt et al.* [2000]). It is important to note that in this first set of numerical experiments, the topography is kept constant since all the samples come from valley floors and therefore cannot be used to constrain the evolution of the topography.

[35] Figure 9 shows results from model runs generated by the GA (10,000 forward model runs). All model runs are represented in the parameter space. Each dot is a single forward model run, and the color of each dot is a function of the percentile value so that smaller percentiles (red dots) correspond to small misfit values.

[36] Misfit reduction leads to convergence of GA toward several optimal values for the horizontal convergence velocity within a range of $5-15$ mm yr^{-1} and $5-35$ km for the listricity. This value of the listricity approximately correspond to a surface dip of $55-15°$ for the Alpine Fault, which includes the range of values described by *Davey et al.* [1995]. Figure 9b also shows a positive linear relationship
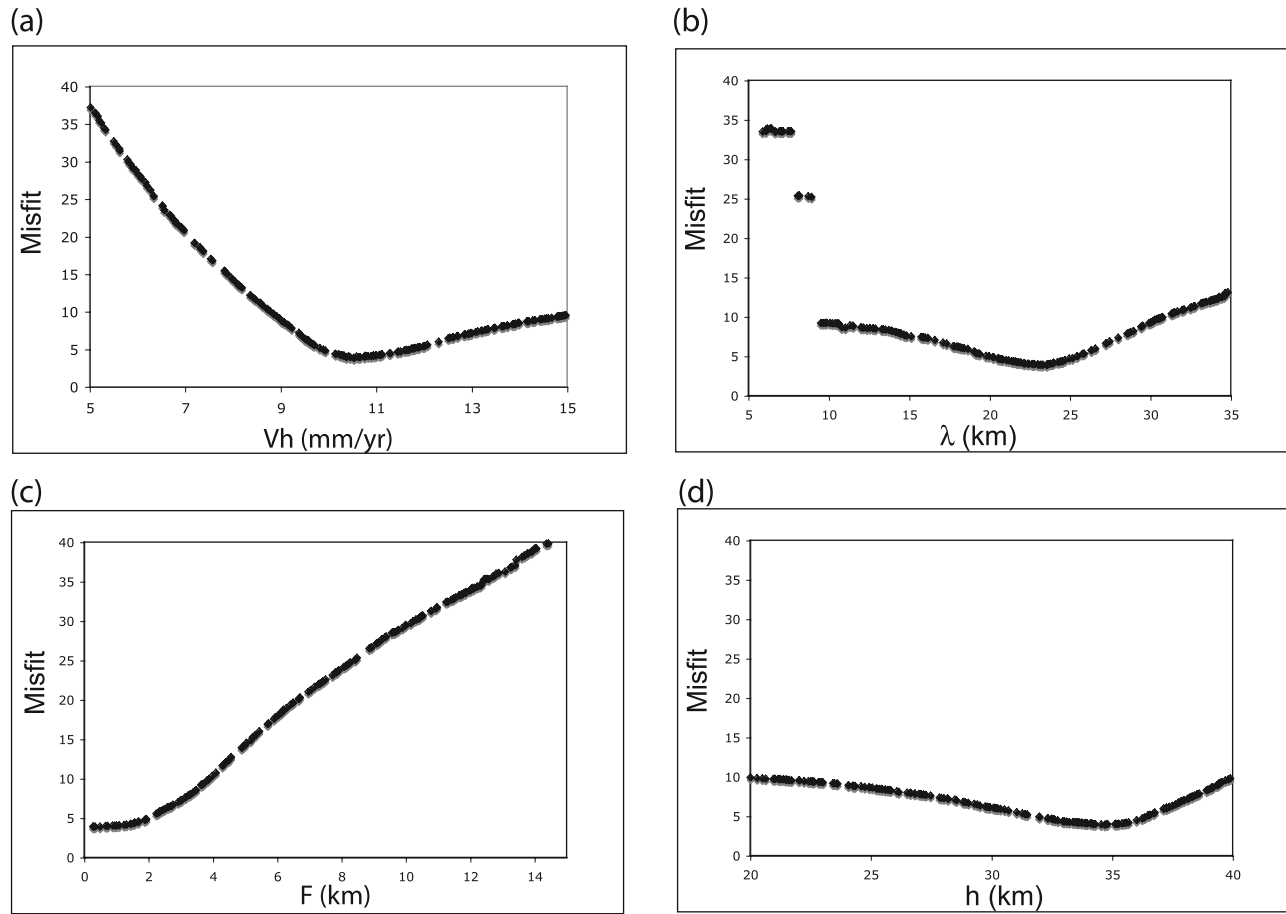
Figure 11. (a) Sensitivity of the misfit function to changes of v_h. The misfit is more sensitive to a reduction of v_h than for an increase. (b) Sensitivity of the misfit function to changes of λ. (c) Sensitivity of the misfit function to changes of F. (d) Sensitivity of the misfit function to changes of h.

between v_h and λ for the best models (red dots). This suggests that the thermochronological data could be equally reproduced in model runs in which the advection velocity is inversely related to the dip of the fault. This is expected with this kinematic model. Indeed, the uplift component decreases as the fault is flattened and, in turn, less heat is advected toward the surface. Similarly, the thickness of the crust h also shows a trade-off with v_h (Figure 9c), suggesting that if the crust is thicker, the vertical heat advection must be faster. Figure 9d also shows that best fit is obtained for small values of F, so that there is no need to include friction along the fault.

[37] We show in Figure 11 the sensitivity of the model to parameter changes. To do so, one parameter at a time is varied while the others are kept equal to the value which leads to the lowest misfit. Figure 11a shows that the misfit function is more sensitive to a reduction of v_h than to an increase. This explains why a large amounts of forward runs lead to a reasonable misfit, yellow dots, in Figures 9b and 9d. Figure 11b illustrates that an increase of λ, with v_h constant, leads to larger misfit values. Figure 11c highlights that the drag along the Alpine Fault must be minimized to obtain a good fit to the data. Finally, Figure 11d shows that the misfit function is not as sensitive to different crustal thicknesses above the decollement but suggest an optimum,

i.e., minimum value of the misfit, for h ~35 km. This optimal value seems to slightly overestimate the base of the decollement which has been imaged about 25 km [*Wannamaker et al.*, 2002]. Finally, the misfit value appears to be mostly sensitive to change in v_h (or F) than in λ and h.

[38] Note that the thermal model used here is limited by the fact that no heat production by shear heating and/or, more importantly in our case, no fluid circulation are considered. The quantitative results must be interpreted carefully, since fluid circulation is an important factor in the Southern Alps [e.g., *Craw*, 1988; *Koons et al.*, 1998]. On the contrary, large amounts of frictional heating seem unlikely [*Shi et al.*, 1996].

5.2. Implications of the Kinematic Model Across the Orogen, Direction Normal to the Alpine Fault

[39] For each thermochronometric system a zone of young ages is observed in the vicinity of the fault. Ages become older while moving away from the fault and toward the southeast. Figure 12 (left) represents the topography on which age predictions are overlaid. The height of the red bars represents measured ages and the blue bars stand for the ages predicted by Pecube. Figure 12 (right) shows the same ages, stacked against the distance to the Alpine Fault. For biotite (Figure 12a), a very good fit is obtained for most
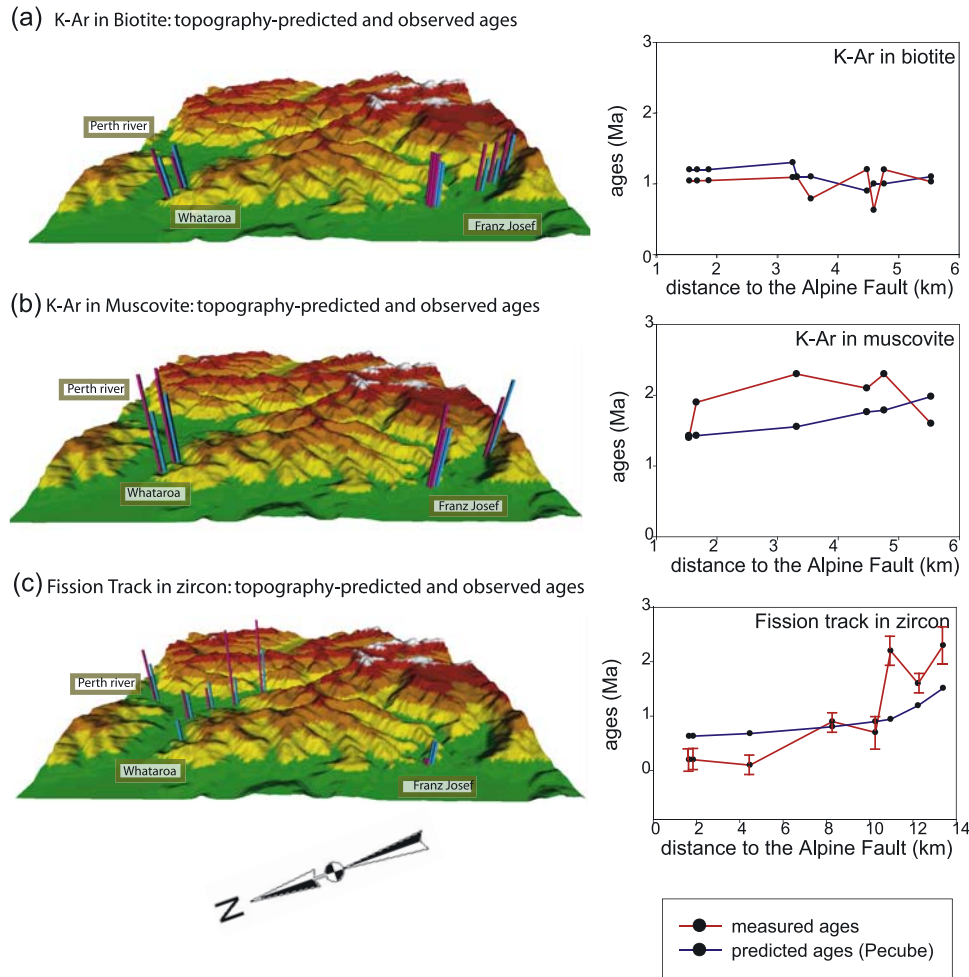
Figure 12. Results of a model run with a set of parameters that produces a good fit to data from *Batt et al.* [2000] and *Kamp and Tippett* [1993] data. The parameters are as follows: $\lambda = 20$ km, $h = 32$ km and $v_h = 9$ mm yr^{-1}. The grid at the surface is taken as $\Delta x = \Delta y = 1$ km. (left) Topography of the central part of the Southern Alps extracted from a digital elevation model (Terralink) on which predicted and observed ages are located and compared. Blue bars are predicted ages and red bars observations. (right) Predicted and measured ages versus distance to the Alpine fault. Ages are in Ma and distance is in km. A general agreement appears for all the thermochronometers, along strike as well as perpendicular. No major difference in regional tectonic regime can be observed with these data, a regime which appears to remain uniform across this area.

of the samples. A good agreement between data and predictions for K-Ar in muscovite (Figure 12b) and fission track in zircon (Figure 12c) is also observed. In the vicinity of the fault, predicted zircon fission track ages are slightly overestimated while biotite and muscovite ages tend to be slightly underestimated. Our simulations show a very high thermal anomaly predicted for this region with a geothermal gradient of $\sim$150°C km^{-1} as a result of heat advection. This is in good agreement with previous numerical simulations [*Koons*, 1990] and heat flow determinations in the Southern Alps [*Shi et al.*, 1996].

5.3. Along-Strike Implication of the Kinematic Model: Geometry of the Metamorphic Isograds and Thermochrons

[40] In the Southern Alps the distribution of thermochrons (i.e., location of rocks that have experienced similar

T-t paths [*Harper*, 1967]) as well as metamorphic isograds east of the Alpine Fault has been inferred to be an expression of spatially varying exhumation rates of crustal material [*Batt et al.*, 2000] during the Late Cenozoic period. *Batt et al.* [2000] interpreted an apparent age increase from Fox Glacier toward the southwest as resulting from a monotonic decrease of the convergence component of the AUS-PAC velocity (Figure 4) [*Beavan et al.*, 2002]. However, this interpretation is contradicted by the thermochrons and metamorphic isograds that are wider northeast of Franz Josef (Figure 13) despite an apparent increase in convergence velocity derived from contemporary velocity field measurement [*Beavan et al.*, 2002] (Figure 4). Interestingly, this widening of isograds also corresponds to variations in the topography. As shown in detail in Figure 13, discrete steps in the position of the Main Divide are observed where thermochrons and isograds widen and narrow. We postulate
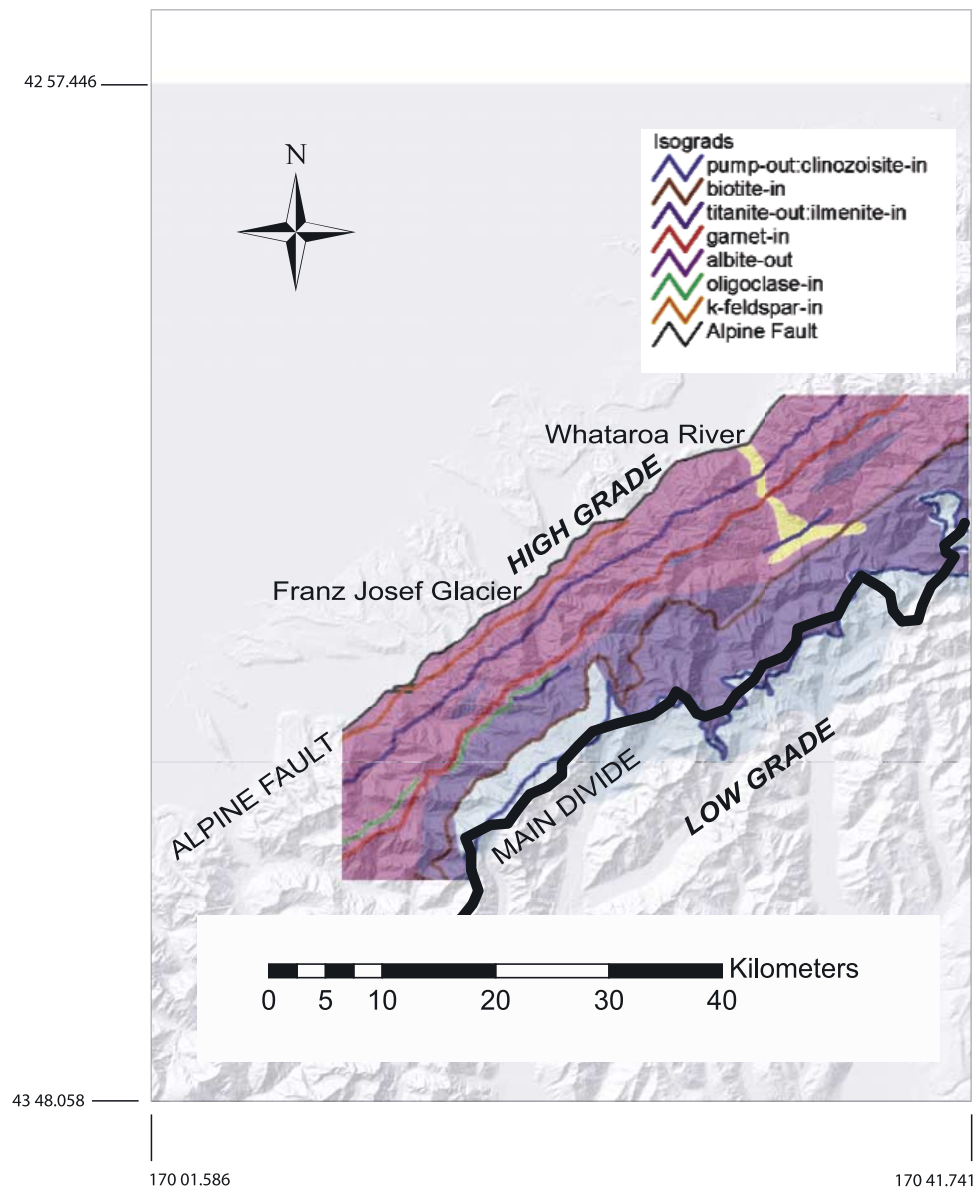
Figure 13. Map showing the strong correlation between the patterns of the isograds and the topography. In the north (Whataroa River), the divide is further away from the Alpine Fault and at lower altitude than in the south (Franz Josef Glacier), while the metamorphic isograds are further apart in the north than in the south. The solid color scheme corresponds to the geology presented in Figure 4.

that the along-strike variation in distribution of thermo-chrons and isograds are partly controlled by the topography.

[41] To demonstrate this point, we have performed two similar numerical experiments using simple, first-order geomorphic scenario. In the first experiment, we compute the variations in thermochron geometry caused by an abrupt change in topography along the strike of the orogen. In one half of the model, the topography resembles the broad scale features of the south Island in the vicinity of Mount Cook, whereas in the other half the topography is nil (flat surface). The geometry of the thermochrons (for the (U-Th)/He system) as predicted by the model is shown in Figure 14a (right): the region of reset ages is wider where the topog-raphy is flat. In the second experiment (Figure 14b) a similar scenario was imposed except that until 300 kyr
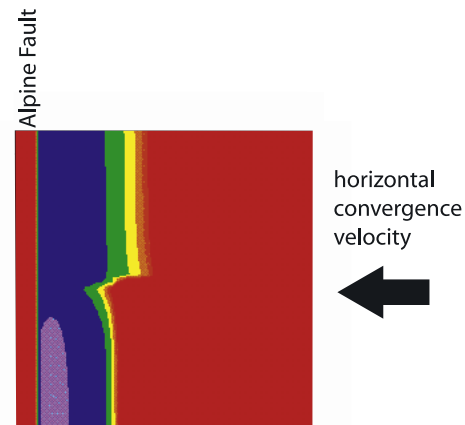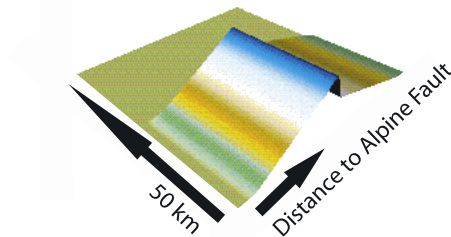
before the end of the model run, the topography was uniformly high. It is only in the last 300 kyr of the model run that the topography in the upper half of the model is progressively eroded away. The effect is even stronger: the region of reset ages is much broader where the topography has been eroded away. These simple simulations demon-strate that the large-scale features of the landform and the rate at which they may have evolved through time might influence the distribution of thermochrons.

[42] This result is expected if one takes into account the effect of both uplift and horizontal advection of rocks. This is shown in Figure 15, by comparing rocks (rocks 1 and 2 in Figure 15) whose final positions are equidistant from the fault but at different altitudes. It shows that rocks which are at lower altitude (rock 2) in the present-day topography

Map of (U-Th)/He ages in zircon predicted by Pecube at the surface.

(a) Topography remains steady at all time

Initial topography = Final topography

Alpine Fault

horizontal convergence velocity

50 km

Distance to Alpine Fault

(b) Upper part of the topography is eroded over the last 300 kyrs of the numerical simulation

Initial topography

Alpine Fault

horizontal convergence velocity

50 km

Distance to Alpine Fault

Final topography

50 km

Distance to Alpine Fault

elevation (km)

0 0.5 1 1.5 2 2.5 3 3.5 4 4.5 5

(U-Th)/He ages in zircon (Ma)
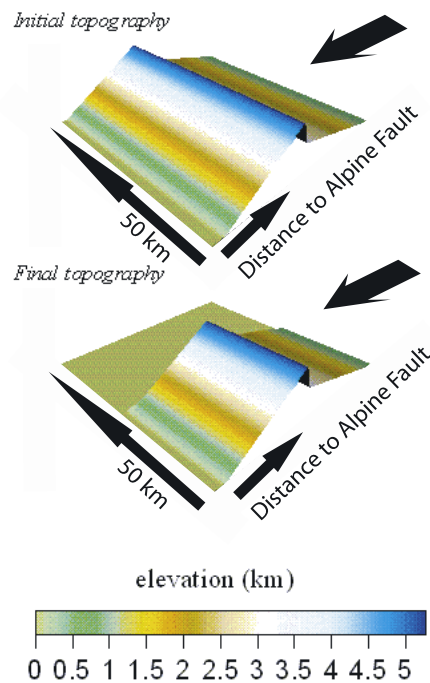
0 0.5 1 1.5 2 2.5 3 3.5 4 4.5 5
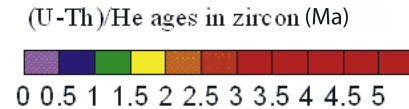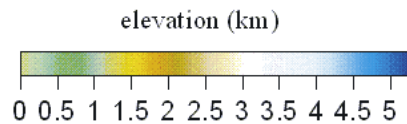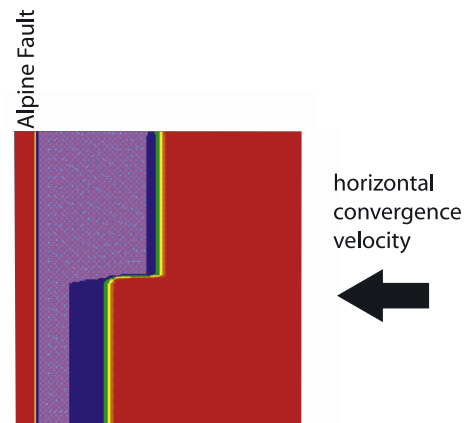
Figure 14. (a) Thermochrons are wider where the topography is flatter, even though this latter does not evolve through time. (b) This effect is reinforced if the flat area represents a region that has been recently eroded.

have been exhumed from deeper in the crust than rocks at higher altitude (rock 1). This suggests that geographical variations in thermochron/metamorphic isograd patterns across a mountain belt can be related to either the rate at which the rocks are tectonically exhumed or the shape of the surface topography and the way it has evolved through time.

[43] *Craw et al.* [2004] and *Herman and Braun* [2006] have suggested that divide migration, or jump, may occur in the Southern Alps. The timing of these events is not well constrained but is thought to happen on very short timescales (less than 100 kyr). This could be a mechanism that triggers very high erosion rates, and could potentially explain the geometry of the thermochrons and metamorphic isograds. Indeed, where the divide is currently near the Alpine Fault the isograds and thermochrons are closely spaced, whereas where the divide is further away from the Alpine Fault, and then has recently migrated, the region of high metamorphic grade rocks and reset ages is broader.

5.4. Local Geomorphic Model

[44] We now continue further in our interpretation of the thermochronological data set by including the low-T data we collected along a transect parallel to the Alpine Fault (Figure 7). We now investigate whether it can be used to derive constraints on the evolution of the relief in this area
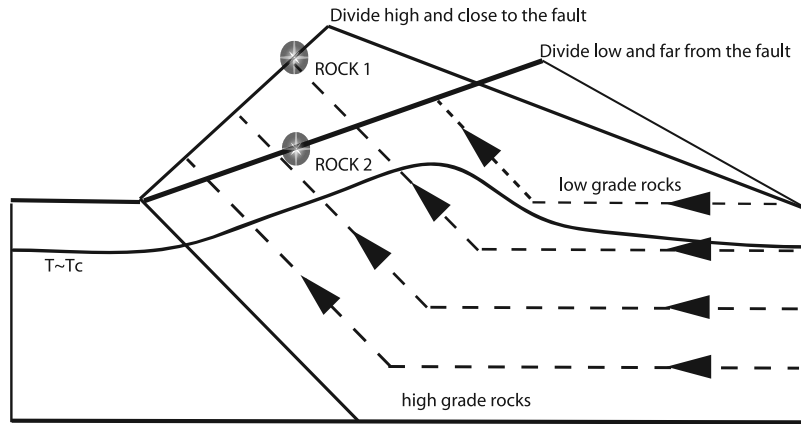
Figure 15. Illustration of the effect of first-order topography on the distribution of the thermochrons. In region where the divide is closer to the fault and higher, the width between each thermochron is narrower than when the divide is lower and further away from the main fault.

of the Southern Alps which, we postulate, should tell us something about the geomorphic evolution of the mountain belt. We assume that a large-scale kinematic model corresponding to a good fit in order to reproduce the mean rock advection and exhumation in the area and proceed to test various geomorphic scenarios ($\lambda = 24.6$ km, $h = 27$ km, $F = 0.1$ km and $v_h = 7.6$ mm yr^{-1}).

[45] We assume that topography at any point varies linearly with time from z_{init} (km) to z_{today} (km) where

$$z_{\text{init}} = z_{\text{offset}} + \left(\frac{z_{\text{today}} - z_{\text{min,today}}}{z_{\text{max,today}} - z_{\text{min,today}}} \right) z_{\text{max,init}} \qquad (10)$$

where $z_{\text{min,today}}$ (= 0.0 km) and $z_{\text{max,today}}$ (= 2.61 km) are the maximum and minimum elevations of the present day relief, z_{offset} and $z_{\text{max,init}}$ are free parameters, z_{offset} varies between 0 and 1 km, and $z_{\text{max,init}}$ varies between 1 and 5 km. These boundaries are chosen so that the relief does not grow faster than what is allowed by the uplift rate, for any t_{init}; z_{offset} represents the base level, whereas $z_{\text{max,init}}$ controls the amplitude of relief. We also perform a parameter search, but we now use the Neighbourhood Algorithm (NA) [*Sambridge*, 1999] to determine the optimum value for z_{offset} and $z_{\text{max,init}}$ and for the time in the past, t_{init}, at which the topography starts changing from z_{init} to z_{today}. The misfit function used in the NA is also defined by equation (9).

[46] Results generated by the NA, after 2460 model runs, are plotted into the [z_{offset}, $z_{\text{max,init}}$, t_{init}] parameter space (Figures 16a and 16b). Lowest values of the misfit function are observed where z_{offset} and $z_{\text{max,init}}$ are both minimized, (i.e., z_{offset} is always small and $z_{\text{max,init}}$ varies between 1.0 and 2.0 km, which is always smaller than 2.61 km). On the contrary, no good constraints can be put on t_{init} (Figure 16a).

[47] Figure 17a shows an example of predicted ages for a set of parameters which provide a low misfit function value (model 1). It clearly shows that overall, predicted ages are close to the observations for both (U-Th)/He and FT ages. The landform change needed to reproduce these measurements corresponds to a local increase of the relief ($z_{\text{max,init}} =$ 1.315 km, $z_{\text{offset}} = 0.0$ km and $t_{\text{init}} = 0.5$ Ma). If β is defined as the ratio between relief amplitude now and at the time in the past where the relief starts changing, our mean optimal

value of $z_{\text{max,init}}$ (1.5 km) corresponds to a $\beta = 1.74 \pm 0.4$ which means that the local relief has increased sometime in the past during the last 1.5 Myr.

[48] We compare in Figure 17b a good fit forward model (model 1) to forward models which lead to larger values of the misfit function (models 2 and 3). Model 2 corresponds to a steady state landscape. It appears that most of the ages are similar along the profile. In model 3, we simulate a situation in which the relief decreases ($z_{\text{max,init}} = 4.0$ km, $z_{\text{offset}} = 0.0$ km and $t_{\text{init}} = 0.5$ Ma). This situation also leads to a poor fit to the data.

5.5. Effects of Horizontal Advection of the Landscape

[49] In section 5.4, the topography in our model was not horizontally advected. However, it has been shown that landscape advection due to horizontal motion may be an important feature of the Southern Alps of New Zealand [e.g., *Willett et al.*, 2001; *Craw et al.*, 2004; *Herman and Braun*, 2006]. This is particularly important near the drainage divide since, in this part of the orogen, the tectonic horizontal advection may be greater than the incision rate. Furthermore, if a topographic feature from the east, where the uplift rate is lower, is advected toward the western side, a relief change should be expected. In the case of the Whataroa-Perth catchment, advection of topography could potentially have important consequences. Indeed, if a large geomorphic feature is to be advected through the drainage divide, the size of the catchment on the west side of the orogen would increase which would cause the divide to migrate away from the Alpine Fault [*Craw et al.*, 2004; *Herman and Braun*, 2006].

[50] In our model, we approximate this by computing the vertical advection with respect to the fault only and progressively advecting the fault at a convergence velocity v_h as sketched in Figure 18. In this way we simulate a situation where the landform is advected with the rocks. In Figure 17b, we compare the (U-Th)/He in zircon ages to the situation where the fault is fixed. This model interestingly leads to a reasonable fit to the data. Although this forward run does not produce as large differences in ages with elevation than in the situation where the topography is
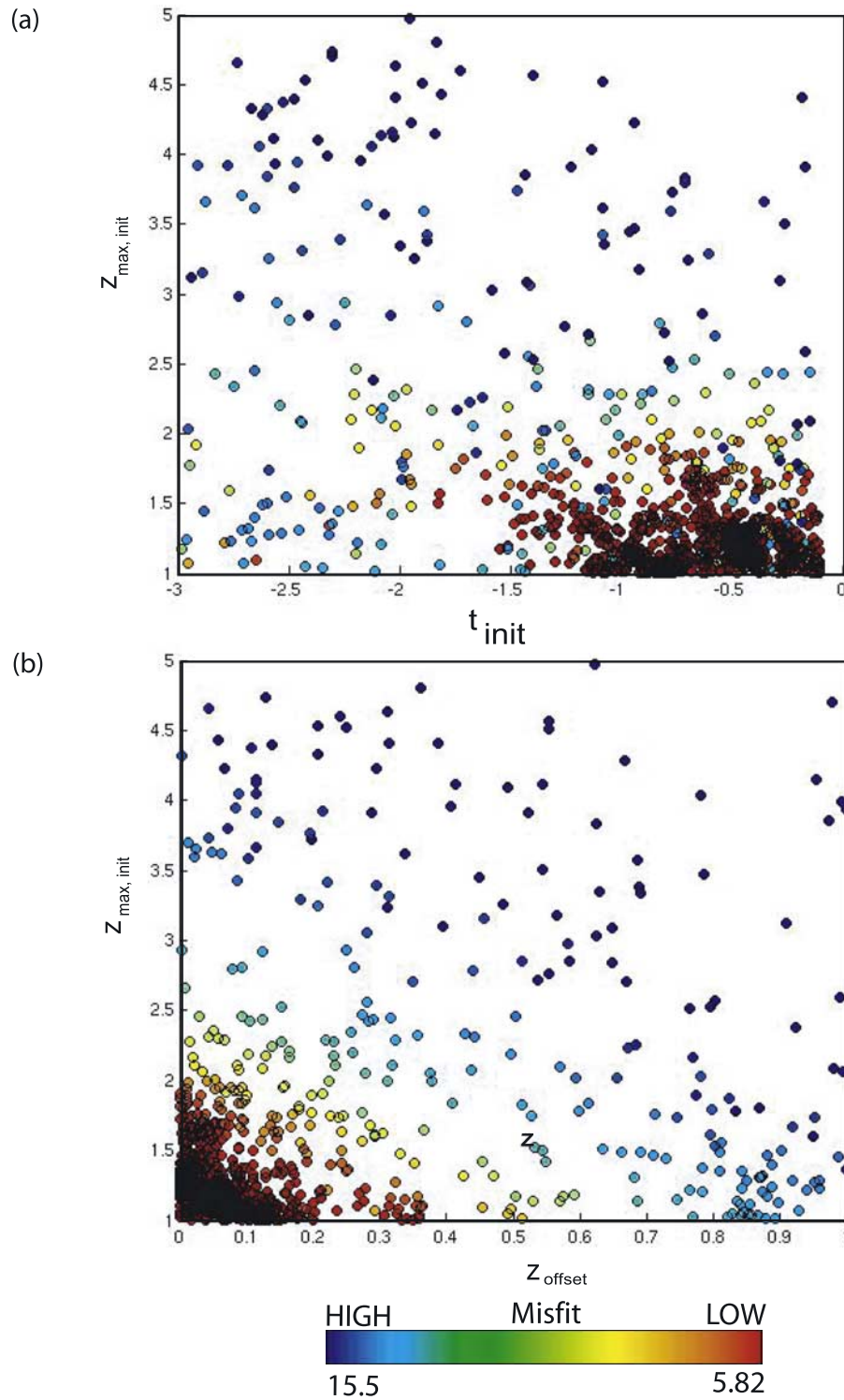
Figure 16. (a) and (b) Calculated misfit into the (z_{offset}, $z_{max,init}$, t_{init}) parameter space (see text).

fixed with respect to the Alpine Fault (Figure 17b), the misfit obtained is comparable to model 1.

6. Spectral Analysis of AER

6.1. Overview

[51] As illustrated in Figure 1, for a given thermochronometric system, there exists a critical wavelength (ω_c) below which topography has little impact on the shape of the isotherms. Consequently, the slope of the relationship between age and elevation data collected at a scale smaller than ω_c provides an accurate estimate of the exhumation rate (Figure 1a). On the other hand, at wavelengths much larger than ω_c, the closure temperature isotherm follows the shape of the topography so that there is no change in age with elevation (Figure 1b).
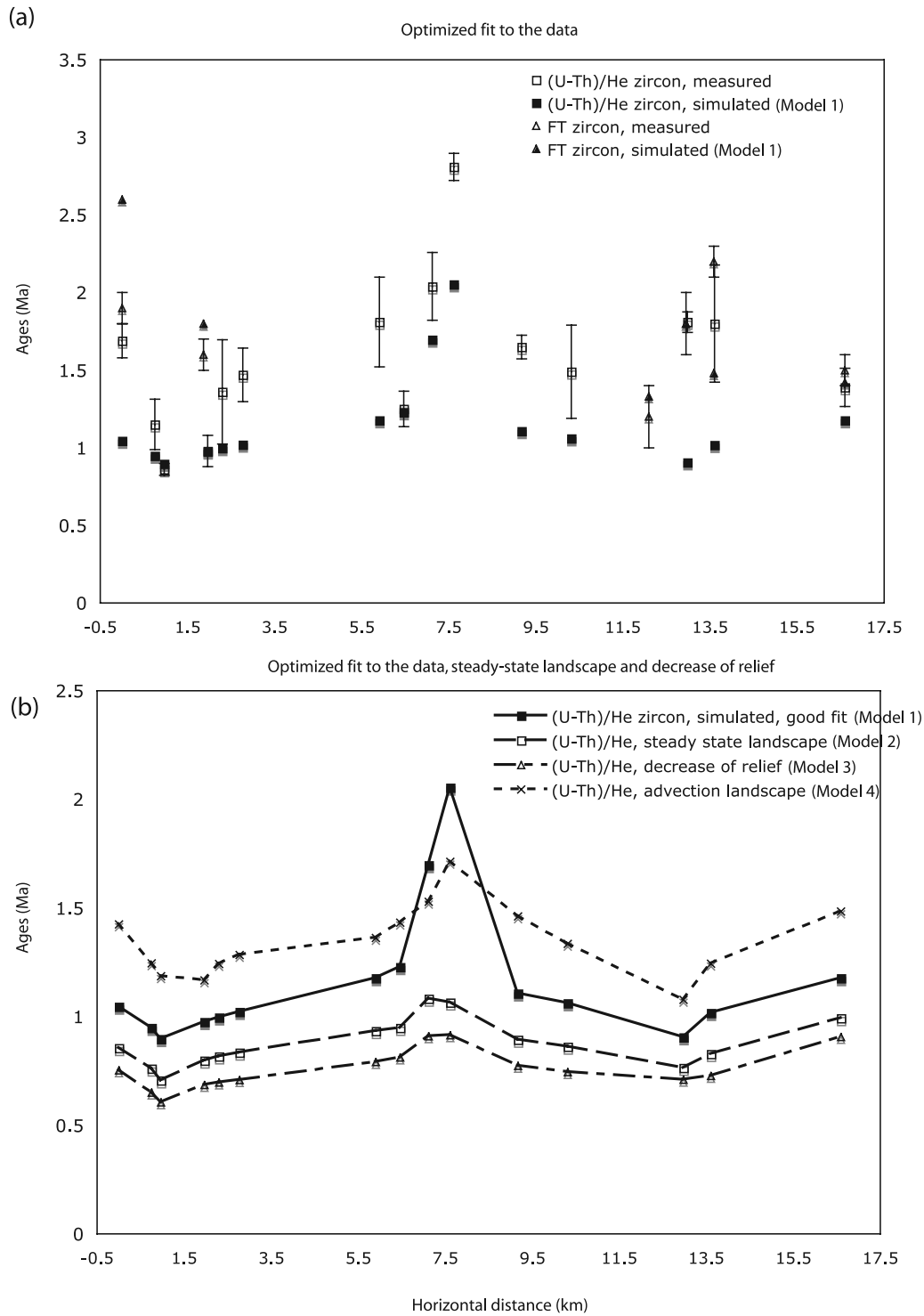
Figure 17. (a) and (b) Forward model results: model 1, model 2, model 3, and model 4 are the results from a simulation with different values of z_{offset}, $z_{max,init}$ and t_{init}. Only (U-Th)/He in zircon ages are shown in Figure 17b for clarity of the figure. Model 1: best fit model (i.e., relief increase during the last 0.5 Myr and fixed topography) (misfit = 5.82); model 2: steady state topography (misfit = 9.97); model 3: decrease of relief (misfit = 12.19); model 4: steady state relief and advection of the topography (misfit = 6.22).

[52] *Braun* [2002a] used this strong dependency of the slope of age-elevation relationships on the wavelength of the surface topography to develop a new method of analyzing thermochronometric data. The method delivers inde-pendent estimates of exhumation rate and the rate of change of surface landform. This new method takes advantage of the fractal nature of surface topography [*Huang and Turcotte*, 1989], which allows one to sample the relationship
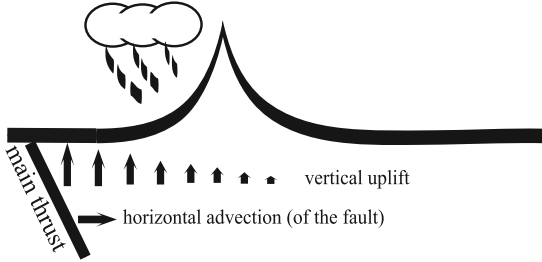
(a) Fixed topography
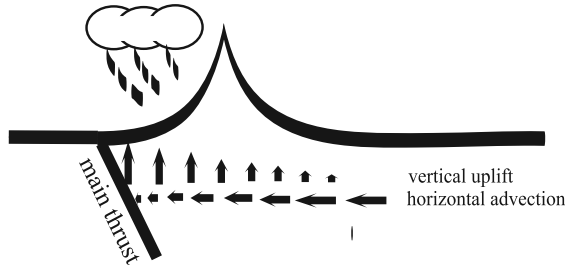
(b) Advection of topography

Figure 18. (a) Simulations with fixed topography (best fit model and model 1). (b) Simulations with horizontal advection (models 2, 3, and 4).

between age and elevation at a wide range of topographic wavelengths by collecting data along one-dimensional transects. Doing so, the problem can be reduced to a spectral system having elevations as input and ages as output. This system can in turn be described by its frequency response function which is expressed in terms of a gain, G (if input and output are in phase: $G = \Re G$), and a phase, F [*Jenkins and Watts*, 1968]. Both are functions of the wavelength of the input topography. *Braun* [2002a] showed that the computed gain function contains two independent pieces of information:

[53] 1. The asymptotic value of the gain at short wavelengths, G_S, provides a direct estimate of the inverse of the mean exhumation rate (E):

$$E = \frac{1}{G_S}. \tag{11}$$

This result is based on the assumption that exhumation rate is constant along the profile.

[54] 2. The asymptotic value of the gain estimate at long wavelengths, G_L, indicates whether, in the recent past, topography has remained constant ($G_L = 0$), has increased ($G_L > 0$) or decreased ($G_L < 0$) in amplitude. As shown in Figure 1c, at very long wavelengths, any gradient in age with elevation must be related to recent changes in surface relief, experienced since the rocks passed through the closure temperature isotherm. β (the ratio between relief amplitude now and at the time in the past) can, in turn, be calculated from [*Braun*, 2002a]

$$\beta = \frac{1}{1 - \frac{G_L}{G_S}} \tag{12}$$

Therefore the ratio G_L/G_S provides a direct estimate of the relative change in surface relief over the time period defined by the mean age of the rocks. This result is based on the assumption that when the rocks pass through the closure temperature isotherm, the temperature field is near steady state; if this is not the case, the ratio G_L/G_S must be regarded as a maximum estimate of the relative change in relief.

[55] Efficient methods exist to compute Fourier transforms from regularly spaced data [*Jenkins and Watts*, 1968]. It therefore requires thermochronological data to be collected at regular intervals along one dimensional transect orthogonal to the main tectonic transport direction. In practice, if regularly spaced interval sampling cannot be achieved, interpolation methods are required. For this to be valid, the condition of uniform exhumation rate along the profile must be met.

6.2. Results

[56] We first projected ages and elevations collected along the profile onto the line that best fits the samples locations, using a classical linear regression. We then use a linear interpolation to provide 64 regularly spaced samples along the straight line (the results of this interpolation are shown in Figure 19), and we calculate the Fourier components for 32 data sets of length 32 each by taking only half of the interpolated data sets and shifting them by one interval for each subdata set (this provides us with 32 estimates of the Fourier coefficients from which statistical estimates, e.g., variance, of G and F can be obtained [*Jenkins and Watts*, 1968]).

[57] At long wavelengths (~8 km), the real part of the gain function, G_L, is clearly positive indicating that the relief has increased over the last 1.5 Myr ($\Re G_{\mathrm{mean}} = 0.6142$, $\Re G_{\mathrm{variance}} = 0.0354$). At short wavelengths, the gain and the spectrum are not well constrained. Another method to estimate G_s must therefore be used. Better constraints could be obtained on G_S by using the slope of the age-elevation relationship (AER) in the Butler River as a proxy for a mean exhumation rate. A linear regression in this part of the transect leads to an estimate of the slope of the AER of 0.83 km Myr^{-1}. This result seems to underestimate the mean integrated exhumation rate in the area. *Brandon et al.* [1998] proposed a method to estimate the mean local exhumation rate. In this calculation, it is assumed that the steady exhumation profile for a one-dimensional layer of thickness h is a function of the exhumation rate [*Stüwe et al.*, 1994]

$$T(z, E) = T_s + g_0 h \frac{1 - \exp\left(\frac{-Ez_c}{\kappa}\right)}{1 - \exp\left(\frac{-Eh}{\kappa}\right)} \tag{13}$$

where g_0 (°C km^{-1}) is the initial geothermal gradient, z_c is the depth of closure and κ (m^2 s^{-1}) is the thermal diffusivity. The cooling rate at closure is a function of the exhumation rate, the closure temperature, T_c, and the vertical temperature gradient

$$\frac{dT}{dt} = \frac{E^2}{\kappa} \left(\frac{g_0 h}{1 - \exp\left(\frac{-Eh}{\kappa}\right)} - T_c + T_s \right) \tag{14}$$
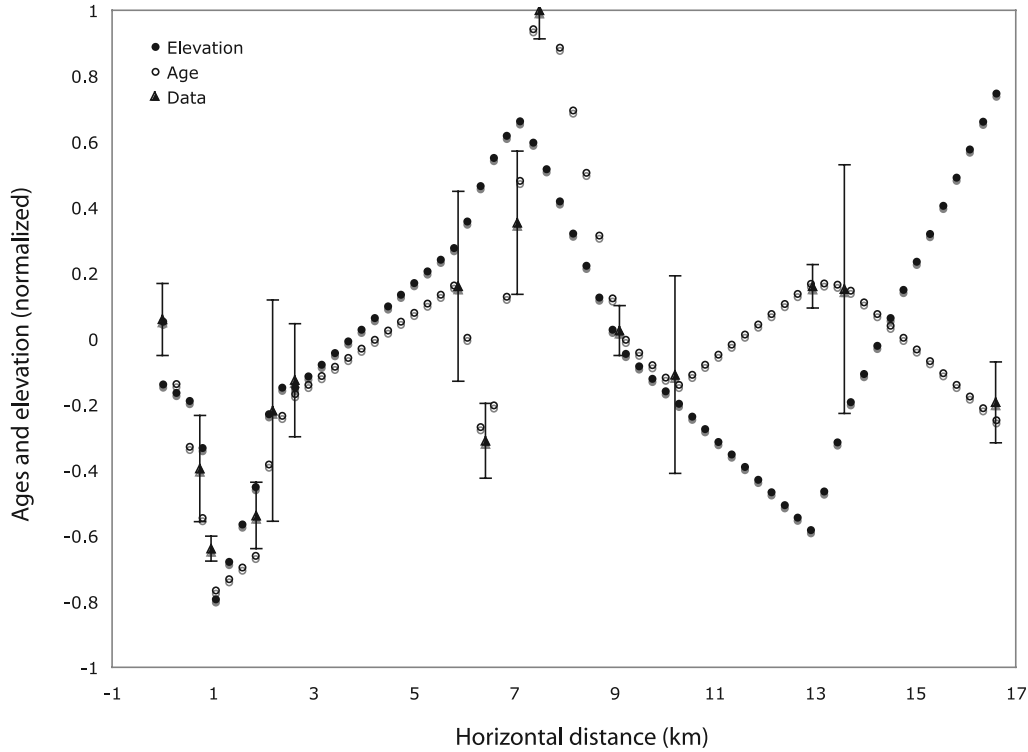
Figure 19. Interpolated ages and elevations along a linear one-dimensional profile.

and in turn

$$z_c = -\frac{\kappa}{E} \ln\left(1 - \frac{T_c - T_s}{g_0 h}[1 - \exp(-Eh\kappa)]\right) \qquad (15)$$

and z_c is related to the age t by

$$z_c = Et \qquad (16)$$

For the range of closure temperature between 170°C and 190°C, one obtains a mean exhumation rate varying between 3.75 and 4.25 km Myr^{-1}.

[58] This yields to, using equation (12), $\beta = 1.18 \pm 0.1$. The error includes the variance obtained from the computation of G_L and the variance on the estimation of the exhumation rate. This estimate is smaller than the results obtained with Pecube and NA in the case of a topography that is not horizontally advected, but it also suggests an increase of relief in the area (β is greater than 1.0). Contrary to our thermal modeling, however, this result has the advantage that the estimate of G_L does not to rely on the assumptions made on the value of the past or present geothermal gradient.

7. Relief Change in the Southern Alps

[59] We have shown that different scenarios enable us to reproduce the observed data, and it may be hard to discriminate which one is best because the timing of change is poorly constrained. First, we have shown that if the topography is not advected, an increase of relief seems to be the best solution. This augmentation of relief could be inter-

preted in several ways. For example, it could simply reflect the difference of relief on either side of the divide, which in this case does not require any horizontal advection of the topography. Another important mechanism which might cause increase of relief is glaciation. It is well known that strong glaciations have occurred in New Zealand [e.g., *Adams*, 1980; *Whitehouse*, 1987; *Suggate*, 1990]. Indeed, our modeling results suggest that a twofold increase in relief can happen during a very short period (≤100 kyr). This is permitted because, in this region, uplift and/or exhumation regimes are such that up to 1 km of rocks can be exhumed within a glacial cycle (i.e., 100 kyr). *Adams* [1980], *Whitehouse* [1987], *Hovius et al.* [1997] and *Herman and Braun* [2006] have also suggested that relief seems to decrease during postglacial periods. Therefore glacial/interglacial cycles would prevent the topography from reaching a steady state and the results presented here would also suggest that relief increases during glaciations. However, better constraints on the timing of the relief change are needed to support such an assertion. Finally, we have shown that if the topography is horizontally advected, one cannot put tight constraints on the evolution of the relief.

8. Conclusions

[60] Our modeling of existing and new thermochronological data enables us to address aspects of the tectonic and geomorphic development of the Southern Alps of New Zealand:

[61] 1. We put constraints on the convergence velocity, v_h, the listricity of the Alpine Fault, λ, and the thickness of the crust above the decollement, h. The modeling exercise

suggests linear relationships between convergence velocity and both listricity and crustal thickness. The ability of the model to reproduce the data appears to be strongly controlled by v_h.

[62] 2. Our numerical model shows that along strike variations of the thermochron/isograd patterns may be related to either the rate at which the rocks are exhumed or the geometry of the topography. Erosion may therefore play a critical role in defining changes in geometrical and geological patterns along and across the mountain belt.

[63] 3. We show with two methods that the relief on the retro-side (i.e., west coast) is likely to have increased between 1.5 Ma and today if the landscape is not horizontally advected. However, we cannot put tight constraints on the time frame over which this occurs, but our results might suggest that the change could have happened within a single glacial cycle.

[64] 4. Including the advection of the landform in our model leads to a different interpretation of the low-T thermochronological data set. Indeed, if the landscape is horizontally advected, there is no requirement for having a relief change to successfully reproduce the data.

References

Adams, C. J. (1980), Contemporary uplift rates and erosion of the Southern Alps, New Zealand, *Geol. Soc. Am. Bull.*, *91*, 1–114.

Adams, C. J., and J. E. Gabites (1985), Age of metamorphism and uplift in the Alpine Schist Group at Haast Pass, Lake Wanaka and Lake Hawea, South Island, New Zealand, *N. Z. J. Geol. Geophys.*, *28*, 85–96.

Allis, R. G. (1981), Continental underthrusting beneath the Southern Alps of New Zealand, *Geology*, *9*, 303–307.

Allis, R. G. (1986), Mode of crustal shortening adjacent to the Alpine Fault, New Zealand, *Tectonics*, *5*, 15–32.

Andrews, P. B., I. G. Speden, and I. D. Bradshaw (1976), Paleontological content of Carboniferous-Jurassic Canterbury suite, South Island, Westland, *N. Z. J. Geophys. Geol.*, *17*, 271–299.

Avouac, J.-P., and E. Burov (1996), Erosion as a driving mechanism of intracontinental mountain growth, *J. Geophys. Res.*, *101*, 17,747–17,769.

Batt, G. E. (1997), The crustal dynamics and tectonic evolution of the Southern Alps, New Zealand: Insights from new geochronological data and fully-coupled thermo-dynamical finite element modeling, Ph.D. thesis, Aust. Natl. Unv., Canberra, A.C.T.

Batt, G. E., and J. Braun (1997), On the thermomechanical evolution of compressional orogens, *Geophys. J. Int.*, *128*, 364–382.

Batt, G. E., and J. Braun (1999), The tectonic evolution of the Southern Alps, New Zealand: Insights from fully thermally coupled dynamical modelling, *Geophys. J. Int.*, *136*, 403–420.

Batt, G. E., J. Braun, B. P. Kohn, and I. McDougall (2000), Thermochronological analysis of the dynamics of the Southern Alps, New Zealand, *Geol. Soc. Am. Bull.*, *112*, 250–266.

Beaumont, C., P. J. J. Kamp, J. Hamilton, and P. Fullsack (1996), The Continental Collision Zone, South Island, New Zealand: Comparison of geodynamical models and observations, *J. Geophys. Res.*, *101*, 3333–3359.

Beaumont, C., R. A. Jamieson, M. H. Nguyen, and B. Lee (2001), Himalayan tectonics explained by extrusion of a low-viscosity crustal channel coupled to focused surface denudation, *Nature*, *414*, 738–742.

Beavan, J., et al. (1999), Crustal deformation during 1994–1998 due to oblique continental collision in the Central Alps, New Zealand, and implications for seismic potential of the Alpine Fault, *J. Geophys. Res.*, *104*, 25,233–25,255.

Beavan, J., P. Tregoning, M. Bevis, T. Kato, and C. Meertens (2002), Motion and rigidity of the Pacific Plate and implications for plate boundary deformation, *J. Geophys. Res.*, *107*(B10), 2261, doi:10.1029/2001JB000282.

Brandon, M., and J. A. Vance (1992), Tectonic evolution of the Cenozoic Olympic subduction complex, Washington State, as deduced for fission track as detrital, *Am. J. Sci.*, *292*, 565–636.

Brandon, M., M. Roden-Tice, and J. Graver (1998), Late Cenozoic exhumation of the Cascadia accretionary wedge in the Olympic Mountains, northwest Washington State, *Am. Geol. Soc. Bull.*, *110*, 985–1009.

Braun, J. (2002a), Estimating exhumation rate and relief evolution by spectral analysis of age-elevation datasets, *Terra Nova*, *14*, 210–214.

Braun, J. (2002b), Quantifying the effect of recent relief changes on age-elevation relationship, *Earth Planet. Sci. Lett.*, *200*, 331–343.

Braun, J. (2003), Pecube: A new finite element code to solve the 3D heat transport equation including the effects of a time-varying, finite amplitude surface topography, *Comput. Geosci.*, *29*, 787–794.

Braun, J., G. E. Batt, D. L. Scott, H. McQueen, and A. R. Beasley (1994), A simple kinematic model for crustal deformation along two- and three-dimensional listric normal faults derived from scaled laboratory experiments, *J. Struct. Geol.*, *16*, 1477–1490.

Brown, R. W., M. A. Summerfield, and A. J. W. Gleadow (1994), Apatite fission track analysis: Its potential for the estimation of denudation rates and implications for models of long-term landscape development, in *Process Models and Theoretical Geomorphology*, edited by M. J. Kirby, pp. 23–53, John Wiley, Hoboken, N. J.

Chamberlain, C. P., P. K. Zeitler, and A. F. Cooper (1995), Geochronologic constraints of the uplift and metamorphism along the Alpine Fault, South Island, New Zealand, *N. Z. J. Geol. Geophys.*, *38*, 515–523.

Cox, S., and R. H. Findley (1995), The Main Divide Fault Zone and its role in the formation of the Southern Alps, *N. Z. J. Geophys. Geol.*, *38*, 489–500.

Craw, D. (1988), Shallow level metamorphic fluids in a high rate metamorphic belt, Alpine Schist, New Zealand, *J. Metamorph. Geol.*, *6*, 1–16.

Craw, D., M. S. Rattenbury, and R. D. Johnstone (1994), Structures within greenschist facies Alpine Schist, central Southern Alps, *N. Z. J. Geol. Geophys.*, *37*, 101–111.

Craw, D., E. Nelson, and P. Koons (2004), Structure and topographic evolution of the Main Divide in the Landsborough-Hopkins area of the Southern Alps, New Zealand, *N. Z. J. Geol. Geophys.*, *46*, 553–562.

Davey, F. J., T. Henyey, S. Kleffman, A. Melhuish, D. Okaya, T. Stern, and T. Woodward (1995), A possible crustal reflection from the Alpine Fault Zone, South Island, New Zealand, *N. Z. J. Geol. Geophys.*, *38*, 601–604.

Dodson, M. H. (1973), Closure temperature in cooling geochronological and petrological systems, *Contrib. Mineral. Petrol.*, *40*, 259–274.

Dunlap, W. (2000), Nature's diffusion experiment: The cooling-rate cooling-age correlation, *Geology*, *28*, 139–142.

Dunlap, W., C. Teyssier, I. McDougall, and S. Baldwin (1991), Ages of deformation from K-Ar and $^{49}Ar/^{39}Ar$ dating of white mica, *Geology*, *19*, 1213–1216.

Ehlers, T. A., S. Willett, P. A. Armstrong, and D. S. Chapman (2003), Exhumation of the Central Wasatch Mountains, Utah: 1. Constraints from low-temperature thermochronometry, *J. Geophys. Res.*, *108*(B3), 2172, doi:10.1029/2001JB001708.

Farley, K. A. (2002), (U-Th)/He dating: Techniques, calibrations, and applications, *Rev. Mineral. Geochem.*, *47*, 819–844.

Findley, R. H. (1987), Structure and interpretation of the Alpine Schists in Copland and Cook River Valleys, South Island, New Zealand, *N. Z. J. Geophys. Geol.*, *30*, 138–177.

Gleadow, A. J. W., and I. R. Duddy (1981), A natural long-term track annealing experiment for apatite, *Nucl. Tracks Radiat. Meas.*, *5*, 169–174.

Goldberg, D. (1989), *Genetic Algorithms in Search, Optimization, and Machine Learning*, 1st ed., Addison-Wesley, Boston, Mass.

Grapes, R., and T. Watanabe (1983), Metamorphism and uplift of the Alpine Schists in the Franz-Josef-Fox Glacier area of the Southern Alps of New Zealand, *Eur. J. Mineral.*, *4*, 547–555.

Green, P. F., I. R. Duddy, G. M. Laslett, K. A. Hegarty, A. J. W. Gleadow, and J. F. Lovering (1989), Thermal annealing of fission tracks in apatite 4. Quantitative modelling techniques and extension to geological time-scales, *Chem. Geol.*, *79*, 155–182.

Griffiths, G. A., and M. J. McSaveney (1983), Distribution of mean annual precipitation across some steepland regions of New Zealand, *N. Z. J. Sci.*, *26*, 197–209.

Grindley, G. W. (1963), Structure of the Alpine Schists of South Westland, Southern Alps, New Zealand, *N. Z. J. Geophys. Geol.*, *6*, 872–930.

Hames, W. E., and S. A. Bowring (1994), An empirical evaluation of the argon diffusion geometry in muscovite, *Earth Planet. Sci. Lett.*, *124*, 161–167.

Harper, C. T. (1967), On the interpretation of potassium-argon ages from Precambrian shields and Phanezoroic orogens, *Earth Planet. Sci. Lett.*, *3*, 128–132.

Harrison, T. M., I. Duncan, and I. McDougall (1985), Diffusion of ^{4}0Ar in biotite: Temperature, pressure and compositional effects, *Geochim. Cosmochim. Acta*, *49*, 2461–2468.

Herman, F., and J. Braun (2006), Landform response to horizontal shortening and glaciations: A study in the Southern Alps of New Zealand, *J. Geophys. Res.*, *111*, F01008, doi:10.1029/2004JF000248.

Holland, J. (1975), Adaptation in natural and artificial systems, in *Genetic Algorithms*, Sci. Am., Univ. of Mich. Press, Ann Arbor.

Hovius, N., C. P. Stark, and P. A. Allen (1997), Sediment flux from a mountain belt derived from landslide mapping, *Geology*, *25*, 231–234.

Huang, J., and D. Turcotte (1989), Fractal mapping of digitized images: Application to the topography of Arizona and comparisons with synthetic images, *J. Geophys. Res.*, *94*, 7491–7495.

Hurford, A. J. (1990), International Union of Geological Sciences Subcommission on Geochronology recommendation for the standardization of fission track dating calibration and data reporting, *Nucl. Tracks Radiat. Meas.*, *17*, 233–236.

Jamieson, R. A., C. Beaumont, P. Fullsack, and B. Lee (1998), Barrovian regional metamorphism: Where's the heat?, in *What Controls Metamorphism and Metamorphic Reactions?*, edited by P. Treloar and P. O'Brien, *Geol. Soc. London Spec. Publ.*, *138*, 23–51.

Jenkins, G. M., and D. G. Watts (1968), *Spectral Analysis and Its Applications*, 1st ed., Holden-Day, Boca Raton, Fla.

Kamp, P., and J. Tippett (1993), Dynamic of Pacific plate crust in the South Island (New Zealand) Zone of oblique continent-continent convergence, *J. Geophys. Res.*, *98*, 16,105–16,118.

Kirschner, D., M. Cosca, H. Masson, and J. Hunziker (1996), Staircase ^{4}0Ar/^{3}9Ar spectra of fine grain white mica: Timing and duration of deformation and empirical contraints on argon diffusion, *Geology*, *24*, 747–750.

Kleffmann, S., F. Davey, A. Melhuish, D. Okaya, and T. Stern (1998), Crustal structure in the central South Island from the Lake Pukaki seismic experiment, *N. Z. J. Geol. Geophys.*, *41*, 39–49.

Koons, P. O. (1987), Some thermal and mechanical consequences of rapid uplift: An example from the Southern Alps, New Zealand, *Am. J. Sci.*, *289*, 1041–1069.

Koons, P. O. (1990), The two sided wedge in orogeny: Erosion and collision from the sand box to the Southern Alps, New Zealand, *Geology*, *18*, 679–682.

Koons, P. O. (1994), Three-dimensional critical wedges: Tectonics and topography in oblique collision orogen, *J. Geophys. Res.*, *99*, 13,301–13,315.

Koons, P. O., D. Craw, S. C. Cox, P. Upton, A. S. Templeton, and C. P. Chamberlain (1998), Fluid flow during active oblique convergence: A Southern Alps model from mechanical and geochemical observations, *Geology*, *26*, 159–162.

Little, T. A., and R. J. Holcombe (2002), Kinematics of oblique collision and ramping inferred from microstructures and strain in middle crustal rocks, central Southern Alps, New Zealand, *J. Struct. Geol.*, *24*, 219–239.

Mason, B. (1962), Metamorphism in the Southern Alps of New Zealand, *Bull. Am. Mus. Nat. Hist.*, *123*, 217–248.

Molnar, P., and P. England (1990), Late Cenozoic uplift of mountain ranges and global climate change: Chicken and egg?, *Nature*, *346*, 29–34.

Molnar, P., et al. (1999), Continuous deformation versus faulting through continental lithosphere: Tests using New Zealand as a laboratory for the study of continental dynamics, *Science*, *286*, 516–519.

Montgomery, D. R. (2001), Slope distributions, threshold hillslopes, and steady-state topography, *Am. J. Sci.*, *301*, 432–454.

Norris, R. J., and A. F. Cooper (2000), Late Quaternary slip rates and slip partitioning on the Alpine Fault, New Zealand, *J. Struct. Geol.*, *23*, 507–520.

Norris, R. J., P. O. Koons, and A. F. Cooper (1990), The obliquely convergent plates in the South Island of New Zealand: Implications for ancient collison zones, *J. Struct. Geol.*, *12*, 715–725.

Porter, S. C. (1975), Equilibrium-line altitudes of the late Quaternary glaciers in the Southern Alps, New Zealand, *Quat. Res.*, *5*, 27–47.

Pysklywec, R. N., C. Beaumont, and P. Fullsack (2002), Lithospheric deformation during the early stages of continental collision: Numerical

experiments and comparison with South Island, New Zealand, *J. Geophys. Res.*, *107*(B7), 2133, doi:10.1029/2001JB000252.

Reiners, P. W., K. A. Farley, and H. J. R. Hickes (2002), Helium diffusion and (U-Th)/He thermochronometry of zircon: Initial results from Fish Canyon Tuff (Colorado) and Gold Butte (Nevada), *Tectonophysics*, *349*, 297–308.

Reiners, P. W., T. L. Spell, S. Nicolescu, and K. A. Zanetti (2004), Zircon (U-Th)/He thermochronometry: He diffusion and comparisons with ^{4}0Ar/^{3}9Ar dating, *Geochim. Cosmochim. Acta*, *68*, 1857–1887.

Reyners, M. (1987), Subcrustal earthquakes in the central South Island, New Zealand, and the root of the Southern Alps, *Geology*, *15*, 1168–1171.

Reyners, M., and H. Cowan (1993), The transition from the subduction to continental collision: Crustal structure in the north Canterbury region, New Zealand, *Geophys. J. Int.*, *115*, 1124–1136.

Sambridge, M. (1999), Geophysical inversion with a neighbourhood algorithm-I. Searching a parameter space, *Geophys. J. Int.*, *138*, 479–494.

Shi, Y., R. Allis, and F. Davey (1996), Thermal modelling of the Southern Alps, New Zealand, *Pure Appl. Geophys.*, *146*, 469–501.

Sibson, R., S. H. White, and B. K. Atkinson (1979), Fault rock distribution and structure within the Alpine Fault Zone, *R. Soc. N. Z. Bull.*, *18*, 55–66.

Smith, E. G. C., T. A. Stern, and B. O'Brien (1995), A seismic velocity profile across the central South Island, New Zealand, from explosion data, *N. Z. J. Geophys. Geol.*, *35*, 565–570.

Stern, T. A. (1995), Gravity anomalies and crustal loading at and adjacent to the Alpine Fault, New Zealand, *N. Z. J. Geol. Geophys.*, *38*, 593–600.

Stern, T. A., P. Molnar, D. Okaya, and D. Eberhart-Phillips (2000), Teleseismic P wave delay and modes of shortening in the mantle lithosphere beneath South Island, New Zealand, *J. Geophys. Res.*, *105*, 21,615–21,631.

Stern, T., S. Kleffmann, D. Okaya, M. Scherwath, and S. Bannister (2001), Low seismic wave speeds and enhanced fluid pressure beneath the Southern Alps of New Zealand, *Geology*, *29*, 679–682.

Stüwe, K., and M. Hintermüller (2000), Topography and isotherms revisited: The influence of laterally migrating drainage divides, *Earth Planet. Sci. Lett.*, *184*, 287–303.

Stüwe, K., L. White, and R. Brown (1994), The influence of eroding topography on steady-state isotherms: Application to fission track analysis, *Earth Planet. Sci. Lett.*, *124*, 63–74.

Suggate, R. P. (1990), Late Pliocene and Quaternary glaciations of New Zealand, *Quat. Sci. Rev.*, *9*, 175–197.

Sutherland, R. (2000), The Australian-Pacific boundary and Cenozoic plate motions in the SW Pacific: Some constraints from Geosat, *Tectonics*, *14*, 819–831.

Tagami, T., H. Ito, and S. Nishimura (1990), Thermal annealing characteristics of spontenaous zircon fission track, *Chem. Geol.*, *80*, 159–169.

Tippett, J. M., and P. J. J. Kamp (1995), Fission track analysis of the late Cenozoic vertical kinematics of continental Pacific Crust, South Island, New Zealand, *J. Geophys. Res.*, *98*, 16,119–16,148.

Townend, J. (1999), Heat flow through the West Coast, South Island, New Zealand, *N. Z. J. Geol. Geophys.*, *42*, 21–31.

Turcotte, D. L., and G. Schubert (1982), *Geodynamics: Applications of Continuum Physics to Geological Problems*, 1st ed., John Wiley, Hoboken, N. J.

Turner, F. J. (1933), The metamorphic and intrusive rocks of South Westland, *Trans. N. Z. Inst.*, *63*, 178–284.

Walcott, R. I. (1998), Present tectonics and late Cenozoic evolution of New Zealand, *Rev. Geophys.*, *36*, 1–26.

Wannamaker, P. E., G. R. Jiracek, J. A. Stodt, T. G. Caldwell, V. M. Gonzalez, J. D. McKnight, and A. D. Porter (2002), Fluid generation and pathways beneath an active compressional orogen, the New Zealand Southern Alps, inferred from magnetotelluric data, *J. Geophys. Res.*, *107*(B6), 2117, doi:10.1029/2001JB000186.

Wellman, H. (1979), An uplift map for the South Island of New Zealand, and a model for uplift of the Southern Alps, in *The Origin of the Southern Alps, Bulletin*, vol. 18, edited by R. I. Walcott and M. M. Cresswell, pp. 13–20, R. Soc. of N. Z., Wellington.

Whipple, K. X., E. Kirby, and S. H. Brocklehurst (1999), Geomorphic limits to climate-induced increases in topographic relief, *Nature*, *401*, 39–43.

White, S. H., and P. Green (1986), Tectonic development of the Alpine Fault Zone, New Zealand: A fission track study, *Geology*, *14*, 124–127.

Whitehouse, I. E. (1987), Geomorphology of a compressional plate boundary: Southern Alps, New Zealand, in *Proceedings of the First International Conference on Geomorphology—Part 1*, edited by V. Gardner, pp. 897–924, John Wiley, Hoboken, N. J.

Willett, R. W. (1950), The New Zealand Pleistocene snowline, climatic conditions and suggested biological effect, *N. Z. J. Sci. Technol.*, *32*, 18–48.

Willett, S. D., and M. Brandon (2002), On steady state in mountains belts, *Geology*, *30*, 175–178.

Willett, S., C. Beaumont, and P. Fullsack (1993), Mechanical model for the tectonics of doubly-vergent compressional orogens, *Geology*, *21*, 371–374.

Willett, S. D., R. Slingerland, and N. Hovius (2001), Uplift, shortening, and steady state topography in active mountain belts, *Am. J. Sci.*, *301*, 455–485.

Zaun, P. E., and G. A. Wagner (1985), Fission track stability in zircons under geological conditions, *Nucl. Tracks Radiat. Meas.*, *10*, 303–307.

————————————

J. Braun, Géosciences Rennes, Université de Rennes 1, Block 15 Campus De Beaulieu, F-35042 Rennes, France. (jean.braun@univ-rennes1.fr)

W. J. Dunlap, Research School of Earth Sciences, Australian National University, Canberra, ACT 0200, Australia. (jim.dunlap@anu.edu.au)

F. Herman, Geological and Planetary Science Division, California Institute of Technology, 1200 E. California Blvd., MC-100-23, Pasadena, CA 91106, USA. (frederic@gps.caltech.edu)